

University of Southampton

## Individual Project Final Report

---

### **Design & Manufacture & Testing of A Wing with High Lift Devices**

---

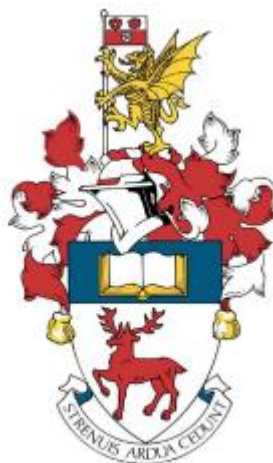
*Written By:* Tan Yee Jie

*Supervised by:* Professor Andy Keane

*This report is submitted in partial fulfilment of the requirements for a  
Master of Engineering*

*Department of Engineering  
Aeronautics and Astronautics*

Word Count: 10286



## **Declaration**

I, Tan Yee Jie declare that this thesis and the work presented in it are my own and has been generated by me as the result of my own original research. I confirm that:

1. This work was done wholly or mainly while in candidature for a degree at this University.
2. Where any part of this thesis has previously been submitted for any other qualification at this University or any other institution, this has been clearly stated.
3. Where I have consulted the published work of others, this is always clearly attributed.
4. Where I have quoted from the work of others, the source is always given. With the exception of such quotations, this thesis is entirely my own work.
5. I have acknowledged all main sources of help.
6. Where the thesis is based on work done by myself jointly with others, I have made clear exactly what was done by others and what I have contributed myself.
7. None of this work has been published before submission.

# **Acknowledgment**

I'm grateful toward my parents about funding me toward my studies and being supportive since the beginning. I thank Professor Andy Keane for offering me the chance of building a test wing and granting me the permission to conduct tests using inside wind tunnel. He had given a lot of practical advise throughout the process and provides me support while doing the computational fluid analysis. The staffs in the wind tunnel also help with sharing their knowledges, experiences, and equipment to complete the tests with some additional visualizations. It has been an absolute enjoyment to be working on this project.

## **1. Abstract**

This project consists of building a testing wing with moving mechanism (high-lift devices) that changes the physical geometry of the wing to maneuver the aerodynamic characteristic of it. The wing is then put into a wind tunnel to conducted tests and aimed for forces reports as the result. The forces report are the representative effects of the high-lift devices and will be discussed in below sections. A further approach is taken using the computational method to compare and discuss the difference between results and provide a closer understanding regarding the flow field around the wing.

# **Contents**

Declaration .....	2
Acknowledgment.....	3
1. Abstract .....	3
2. Introduction.....	6
3. Literature Review .....	6
4. Methods .....	15
4.1 Design of the Wing .....	15
4.1.1 Overall Shape and Size of the Wing.....	15
4.1.2 The Slat's Mechanism.....	16
4.1.3 Flap's Mechanism .....	18
4.1.4 Main Body.....	19
4.1.5 Tapered Body.....	20
4.1.6 Ribs .....	21
4.2 Manufacture of the Wing .....	22
4.2.1 Bodies the Wing.....	22
4.2.2 Ribs .....	22
4.2.3 Slats Mechanism.....	23
4.3 Mounting of the Wing .....	23
4.4 Process of the Testing.....	25
4.5 Processing & Calculations of Wind Tunnel Data .....	26
4.6 CFD Methods .....	28
5. Results .....	32
5.0 Configurations & Terms.....	32
5.1 Main Results .....	34
5.2 Individual Testing for Trailing-Edge Flaps.....	36
5.3 Individual Testing for Leading-Edge Slats.....	39
5.4 Special Combination of Deployment of the High Lift Devices.....	41
5.5 CFD Results .....	42
6 Discussions & Improvements .....	47
6.1 Discussions of the Results .....	47
6.1.1 Wind Tunnel Result .....	47
6.1.2 CFD Result.....	48
6.2 Improvement Made.....	49
6.3 Additional Test (After Improvement are Made).....	55
6.4 Extra.....	58

7. Conclusions.....	59
8. References .....	60

## **2. Introduction**

In the current field of the aeronautical engineering, fluid dynamic take part in an important main role in design and developing. Vital practical in studying the airfoils are indispensable for fluid dynamic. The widely usage of airfoil nowadays includes wing, propellers, wind turbines etc. This has led to a highly demanding field of research regarding improvement that can made toward current airfoil to compensate the different usage that it can be applied on. The consideration that needs to be made includes the aerodynamic characteristic such as the lift & drag, the stall characteristic etc. The flow phenomena around the airfoil inclusive of the vortex formation, vortex shedding, flow separation, turbulent is the direct cause of the performance that an airfoil can produce.

As the air commercial transportation industry are becoming the one of the main methods of traveling, the low speed/high lift performance will be a primary safety issue. This performance issue also held responsible for a major constraint regarding the overall performance and the sizing of an aircraft. Thus, to resolve the issue, one of the key improvisations that can be made toward an airfoil is splitting them into several components that form the “high-lift device/system”. High-lift system introduce high impacts toward the aircraft operating cost, the usage of carbon-base fuels and more (R. Radespiel, *High-lift research for future transport aircraft*). Thus, the high-lift device is an important topic to investigate into in order to understand better towards the aeronautical field.

## **3. Literature Review**

The lift generated from an airfoil is mainly affected by the pressure difference between the upper and lower surface of it. It is defined as oppose the direction of gravity and does not change its vector direction with the inclined angle of the airfoil. For lift to be generated, the upper surface must have lower pressure than the lower surface. Only then there will be a net force acting upwards. To produce the pressure difference, the airfoil must satisfy either cambered or angled relative to the flow direction or both. As shown in figure below, the airfoil can be either symmetric, positively camber and negatively camber. Symmetric airfoil can only generate lift when at an inclined angle (angle of attack) with the incoming flow direction. At zero angle of attack, the lift/lift coefficient of the airfoil will be exactly zero. Positively camber airfoil can generate lift even at zero inclined angle with the incoming flow. Thus, it is widely applied in the

design of a wing. By varying the camber of the airfoil, it is also possible to improve stall and stall recovery characteristic.

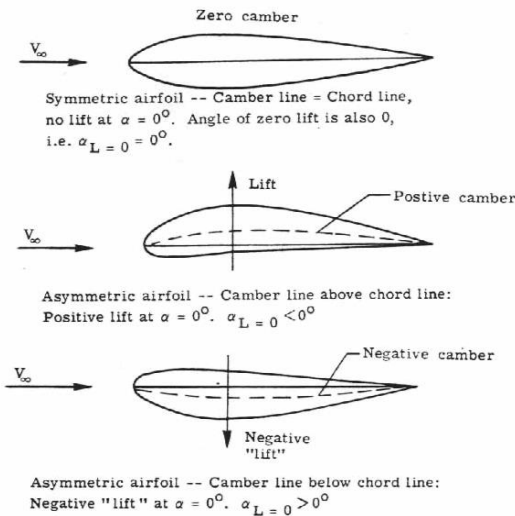


Figure 3.1: Airfoil Shape [2]

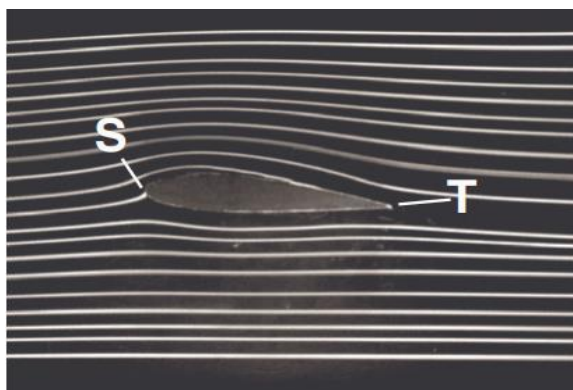


Figure 3.2: Streamline of an Airfoil Visualized with Smoke. [3]

Figure 3.2 shows a visualized streamline of the flow over an airfoil. In the figure, S indicates the stagnation point or leading edge of the airfoil which flow are split into the upper and lower surface of the airfoil, T indicates the trailing edge of the airfoil. The most popular explanation regarding how lift generated is stating the velocity of the upper surface is higher than the lower surface. The argument circles an important assumption that the neighbouring flow particle that split at the leading-edge should meet again on the trailing edge. According to the assumption, as the distance on the upper surface of the airfoil from S to T is longer than the lower surface, the velocity of the fluid on the upper surface must be higher than the lower surface. Quoting the Bernoulli's equations, the higher the velocity the lower the pressure and so lift is gained.

The argument above relies highly on the assumption made about the neighboured flow particles reunited at the trailing-edge. However, it is proven to be unreliable. Figure 3.3 below is a GIF showing that the flow particles doesn't necessarily reunite at the trailing-edge (sourcing available at reference).

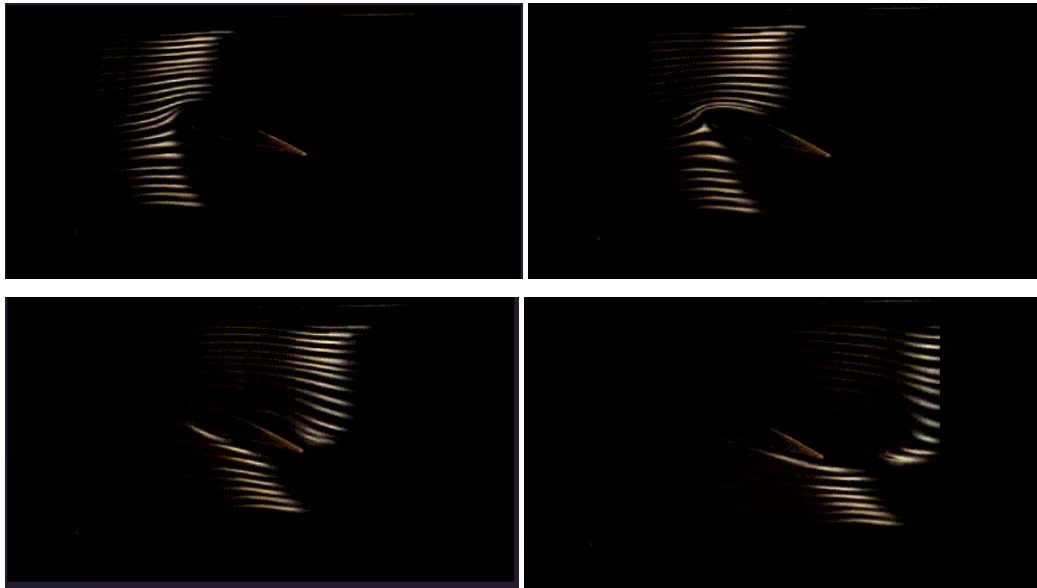


Figure 3.3: Flow over Airfoil Visualized by Smoke. [3] (Available at: <https://drive.google.com/drive/folders/1P4qg24GLAZOsEQ3WN4YksWxod3BD3EWg?usp=sharing>)

An alternative explanation of the lift generation can be start from assuming the no friction force except close to the solid surface (boundary layer), and steady flow.

Applying Newton's second law, a force acting in the flow direction will result in change in fluid velocity, force acting normal to flow direction will cause a curvature in the streamline. Due to Coanda effect that state that the flow tends to curve away from its initial direction and follows the curvature of the surface, the streamline around an airfoil tends to follow the curvature of it. Since the flow around the airfoil is curve, this means that there are forces acting normal to the airfoil. In short, this is how airfoil generates lift.

However, there is a maximum amount of lift that can be gained in each condition by a fixed wing as the angle of attack continues to increase. The wing/airfoil will eventually reach its stall limit, increasing angle of attack beyond that point causes the lift generated to drop significantly at an instance. Due to the adverse pressure gradient that grows on the upper surface leading edge, the flow separation point on the upper surface will continue to shift forward towards the leading-edge as the angle of attack increases. After the suction peak, the boundary layer will instantly detach from the airfoil surface due to the high amount of adverse pressure gradient. The airfoil/wing will

then experience the deep stall states, where the flow around the airfoil is no longer steady and stormed with vortices. The angles of attack where stall will happen exceeding it, is called the stall angle. The stall angle is not constant for every airfoil, and it have relations to the airfoil's geometry. Figure demonstrates the flow field around an airfoil experiencing stall. The flow is clearly detached from the airfoil's upper surface.

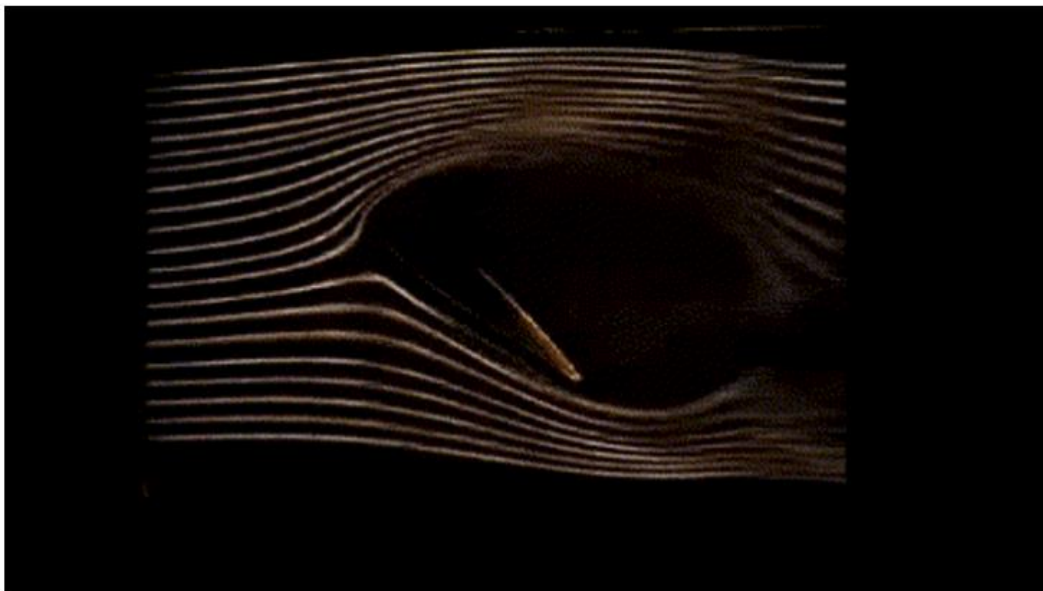


Figure 3.4: Streamline of Airfoil Entering Stall. [3] (Available at:

<https://drive.google.com/drive/folders/1P4qg24GLAZOsEQ3WN4YksWxod3BD3EWg?usp=sharing>)

For airfoil entering stall, other than the sudden drop in lift, the drag of the airfoil is also increased. Drag is defined as oppose the direction of the travel no matter how inclined the airfoil is as shown in figure 3.5 below. Generally, the drag generated by an object moving through air is depended on the shape of it and the way it moves through air. As for airfoils, the drag is nearly a constant at small angle of attack (e.g., plus/minus 5°). As angle of attack increase, the drag also increases. This can be seen as the angle of attack increases, the frontal area of the airfoil increase, resulting in a higher force implied by the fluid. The boundary layer thickness will also increase as the angle increase, which effectively changing the streamline geometry of an airfoil resulting in more drag produces. After the stall of an airfoil, the relationship between drag and angle of attack became more complex as the flow are no longer steady.

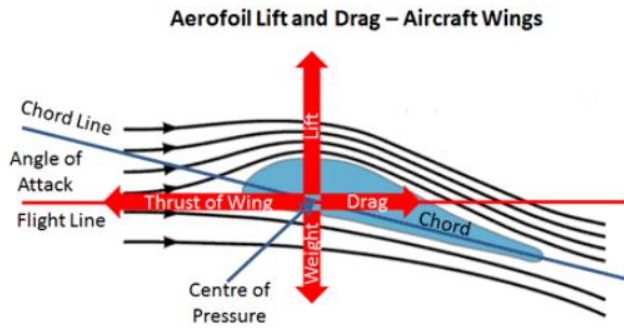


Figure 3.5: Illustration of Forces. [25]

The drag of airfoil can be split into many forms, in different Reynolds number, the dominant drag component will be different. For example, at low Reynolds number, the drag force is normally depended on the skin friction drag. Skin friction drag is caused by the viscosity of the air and the resulting friction with the surface contact of the object. In high Reynolds number, the pressure drag dominates. Pressure drag is the drag caused by the separation of the boundary layer and the wake region due to the separation. After the trailing edge, the greater pressure on the lower surface will exert a force onto the lower pressure flow above, causing vortices to the flow, the pressure after the trailing-edge is decreased. Due to the pressure difference between the frontal area of the leading edge and after the trailing edge, the airfoil forward motion is retarded and resulting in additional drag called the pressure drag.

High lift devices are the components or mechanism that are installed on the wing which can be deployed to gain additional lift. They are often deployed during the needs of performing low speed actions (e.g., take-off, landing). To maximize the fuel efficiency during cruise phase of the aircraft, a smaller wing is often preferred, to reduce the drag. However, the small wing that provides fuel efficiency doesn't necessarily generate sufficient lift during low speed as the lift is governed by the following equation.

$$L = 0.5\rho V^2 S C_L$$

$L$  is the lift,  $\rho$  is the density,  $V$  is the velocity,  $S$  is the reference area of the wing and  $C_L$  is the lift coefficient of the wing. This phenomenon is especially severe when it comes to large commercial jet aircrafts with their swept wings.

To balance the outcome of low lift due to low airspeed, the only sensible change that can be made is to increase the  $C_L$  &  $S$ . Since  $C_L$  is determined by shape of the wing,

increasing it will mean making changes toward the wing's geometry. Figure 3.6 below shows the general demonstration of the slats and flaps deployment.

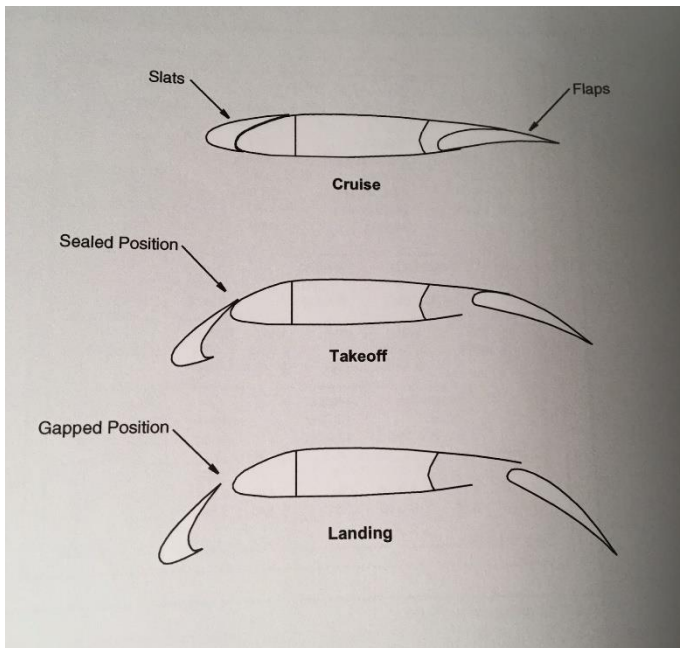


Figure 3.6: Slats and Flaps Deployment. [8]

Referring to Figure 3.6, the slats and flaps effectively change the camber of the airfoil, increasing the  $C_L$  and at the same time increases the reference area,  $S$ . Generally, for large commercial aircraft, the take-off configuration of the wing consists only half deployed slats and flap while the landing configuration utilizes the full deployment of the high lift devices.

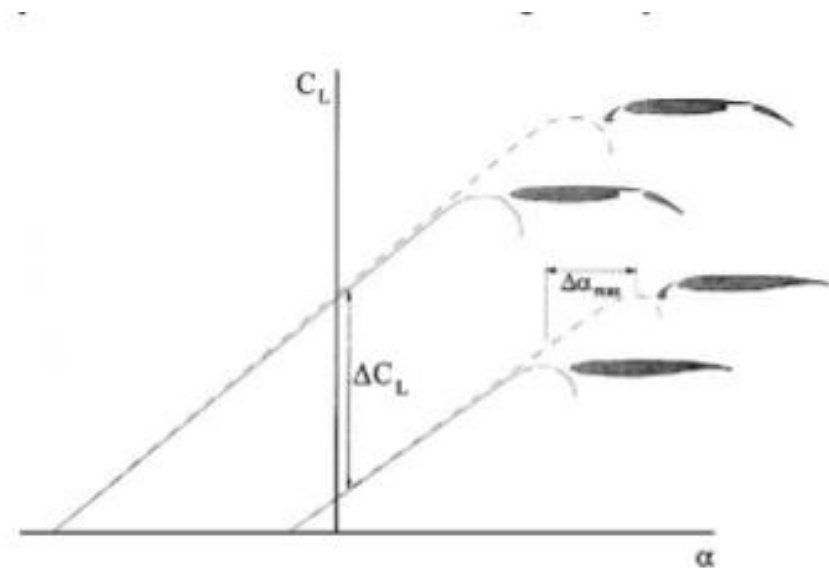


Figure 3.7: The General Effect of High Lift Devices on the Lift Curve Graph. [31]

Breaking down into the individual contribution of the high lift devices, the flaps increase the lift coefficient that the airfoil/wing can achieve at a given angle of attack but at the same time reducing the stall angle, making it easier to step into the stall region. The effect of it on the lift curve graph is shown in figure 3.7. While the increment of lift seems to be complimentary, the deployment of trailing-edge flaps does introduce drag penalty. According to the FAA, flap deflection up to  $15^\circ$  generates mainly lift with minimal drag. Increasing the deflection angle of flaps over  $15^\circ$  will cause a large drag penalty and causes significant nose up pitching moment on high-wing aircrafts. Thus, the flaps are often not fully deployed during take-off as the large drag penalty might result in insufficient thrust to accelerate the aircraft to its take-off speed.

The slats on the leading edge increase the angle of attack before the reaching stall and increase the lift with low drag penalty. The slats are extended out from the main airfoil itself and contained a gap between them as shown in figure 3.6.

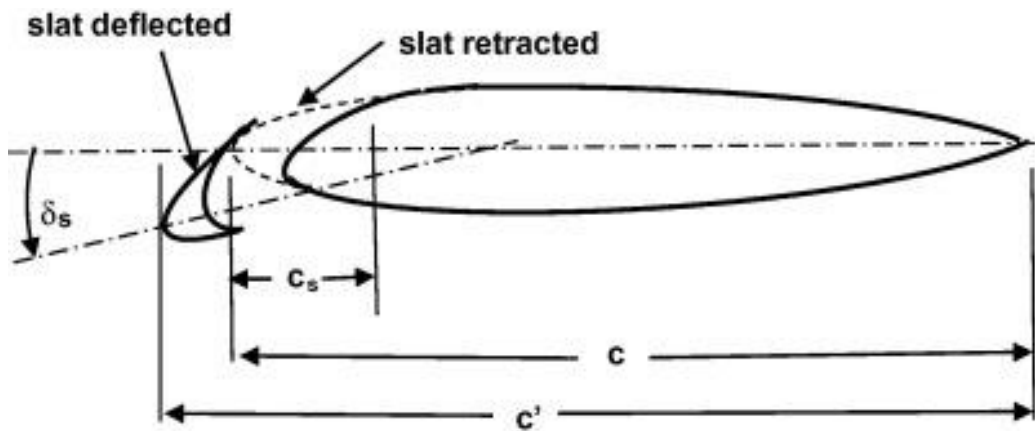
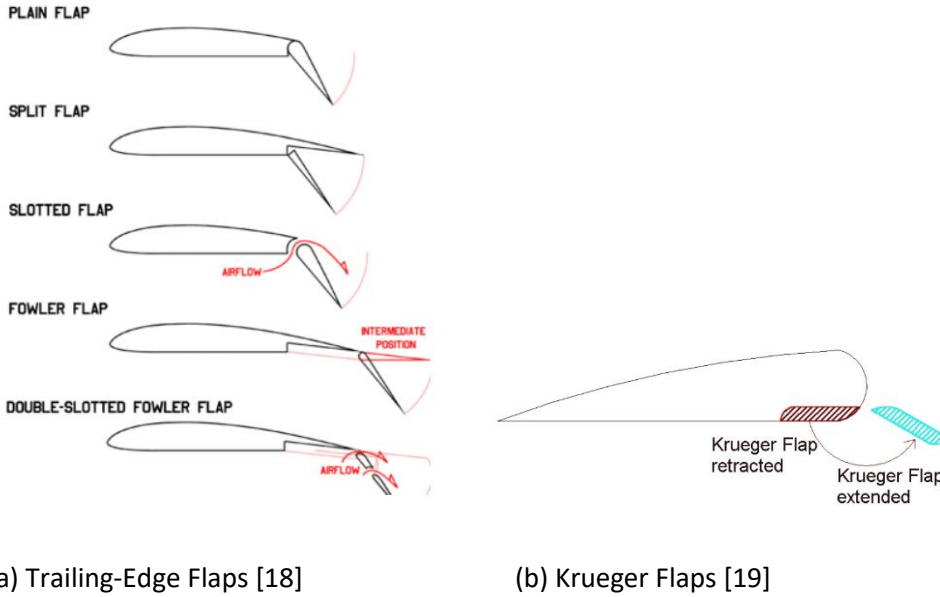


Figure 3.8: Demonstration of Slat [13]

The gap is the key feature in increasing the stall angle. As the slat is deflected from the main body, a portion of high-pressure flow on the lower surface will gain access to the upper surface and allow the mixing of both flows to happen. This will make sure the flow attaches to the surface longer as angle of attack increases which means a later separation point chordwise, delaying the stall. As the slat is deflected, it changes the camber of the airfoil positively and increasing the  $C_L$ , like the flaps. The effect of the slat can be visualized on figure 3.8 above. To achieve optimal lift with less drag while avoiding stall, the combination between both is often opt for.

Digging down toward designing a high-lift device, the general constraints includes optimising the design using merit functions based on the weight and complexity to fulfil the requirements. Since most of the wings are optimised for the cruise performance,

the high lift devices must be made with minimal impact toward it. Additionally, designing the high lift devices includes choosing the optimal combinations between the high lift devices. For instance, there are many types of leading-edge and trailing-edge devices, figure 3.9 show an example of type of flaps including a leading-edge flap called the Krueger Flaps.



(a) Trailing-Edge Flaps [18]

(b) Krueger Flaps [19]

Figure 3.9: Type of Flaps

The designs constraints include but not limited to the support and deployment mechanisms required to move the high lift devices to their corresponding position. Other than the light-weighted required for the mechanism, it is critical that the mechanism generates low contributions towards the parasitic drag during the cruise phase due to considerations fuel-cost wise.

Due to the many constraints, designers tend to make use of a 2-D computational fluid dynamics (CFD) during the initial design phase. Still, due to the limited understanding regarding the viscous effects experience by the high lift device, the 2-D CFD provides bounded prediction of the respective force reports. Plus, complex, and accurate CFD often takes out high cost and great amount of time. While the simulation itself takes on a lot of time, a 2D approximation still doesn't account for the 3D effects. For example, the wing-tip vortex that encountered for all real-world wings, contributes a lot towards the unfavorable drag.

The term “high-lift building block flows” implies that the flow field over any multi-element airfoil that is broken down in some generic component flow types [15]. Figure 3.10 demonstrate how the flow are broken down.

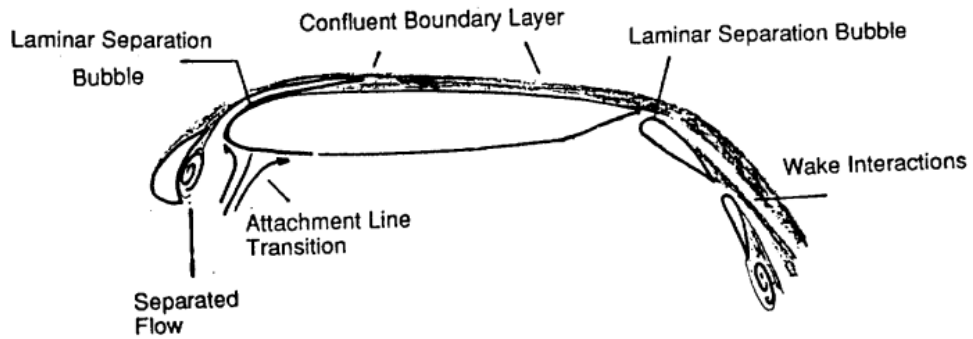


Figure 3.10: High-Lift Building Block Flows. [15]

In a multi-element airfoil, the flow field are strongly coupled. Since the flow field directly affects the performance of the high lift devices, it is useful to study the coupling of the block flows. Wind tunnel testing provides information to fill up the missing components, providing progression towards understanding the flow.

## **4. Methods**

### **4.1 Design of the Wing**

#### **4.1.1 Overall Shape and Size of the Wing**

First out of all is deciding the overall length of the wing, the chord length, the airfoil shape, and the general outline of the wing (i.e., Elliptical, twisted, etc.). Simple simulations and calculations are conducted to compare the aerodynamic performances of most common airfoils. Figure 4.1.1.1 shows the final comparison between the Clark Y airfoil and the NACA4415 using inviscid simulation of the X-FLR5.

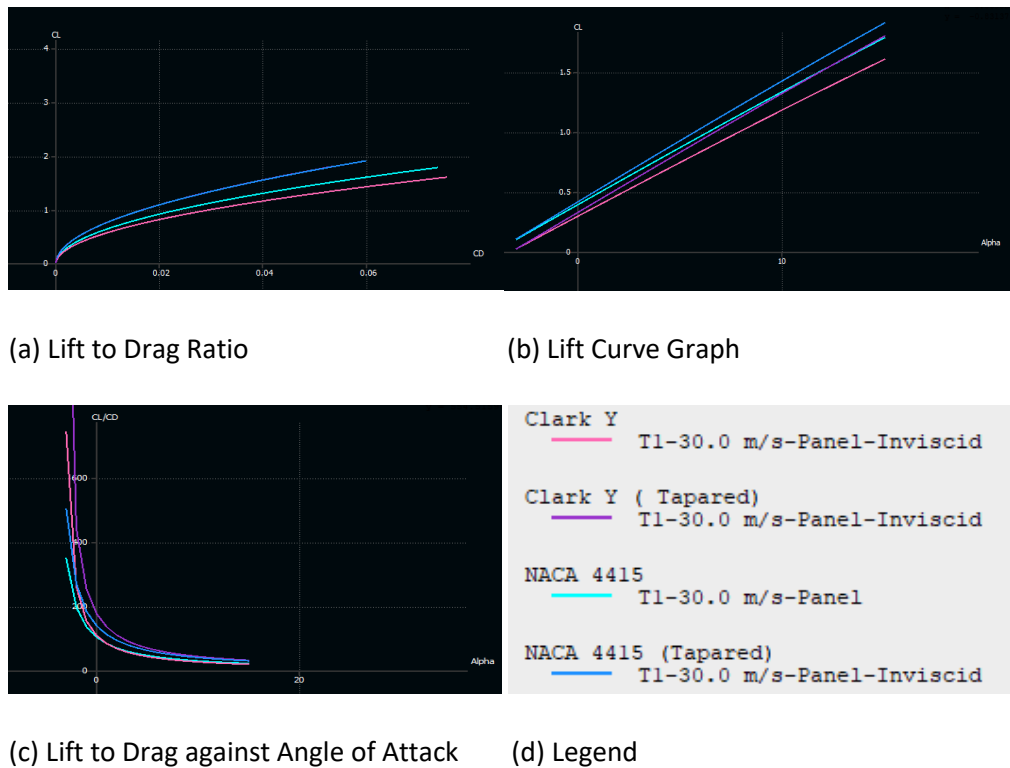


Figure 4.1.1.1: X-Flr5 Simulation of Clark Y & NACA 4415.

The data has resulted in Clark Y airfoil being chosen as the base airfoil. It is widely used in general purpose aircraft designs due to its outstanding lift to drag ratio,  $\frac{C_L}{C_D}$ , and flat lower surface. A flat surface reduces the workload in the manufacturing process and allow an easier alignment for the angle of attack in the wind tunnel. Chord length is determined to be 0.34 metre and further modified to be thicker to enable the internal features for the wing (i.e., main spar, mounting points for slats mechanism, flaps mechanism, etc). The modified airfoil has maximum thickness of 17.27% in relative to chord at 27% chord, Figure 4.1.1.2 shows the exact dimension of the airfoil that will be used.

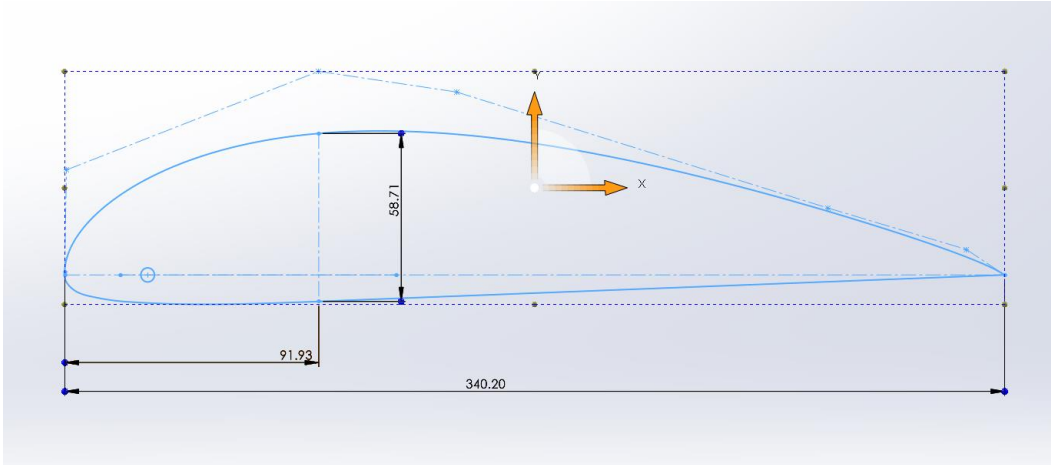


Figure 4.1.1.2: Modified Clark-Y Airfoil.

The wingspan is around 1 metre, excluding the mounting part for the wing to be connected to the wind tunnel's force balance.

The original design is that the wing will be tapered throughout the span. This results in the high lift devices surfaces to possess some form of tapered. This unfortunately introduces the drawback in designing and manufacturing the mechanism of the high-lift devices. It is then replaced by a partially tapered wing with the slats and flaps being rectangular into a tapered mid span towards the wing tip. By completing simple simulations in the X-FLR5, a partially tapered wing is capable to reduce the effect of a wing tip vortices as if the fully tapered wing does as long as the tapered ratio is the same. The tapered ratio, ( $\frac{\text{Tip Chord}}{\text{Root Chord}}$ ) of is 0.5 with root chord being 0.34m and tip chord of 0.17m.

#### 4.1.2 The Slat's Mechanism

Since the leading-edge slats need to have synchronize motion on both side of the mechanism, preserve designs are first considered. To avoid unequalled deployments (e.g., one side deployed more than the other), electronics such as servos indicates complexity and is unnecessary as the wing is made for only wind tunnel testing. The conceptual design is to make a slider mechanism for the slats to slide down to the desired point and fixing it to the desired position (i.e., 10% expansion, etc) using alignments of holes on the slats and the rib of the wing. It was soon replaced as making a smooth slider with both sides synchronize is relatively difficult due to the lack of extreme precision in manufacturing. As a substitute for the slider, a four-bar linkage is applied to the mechanism to enable the slats to extend out from the leading edge and

rotate downwards about the x-axis of the wing. This will introduce a gap between the slat and the body of the wing, enabling favourable flow mixing to happen. The fixing of the slats in position (i.e., different degree of deployment) can be accomplished simply by aligning the holes on the slat with the ones on the rib and slotting a bar through the holes. The hole made for different deployment configuration of the slat are drilled on the secondary rib of the slat, as shown in figure 4.1.2.1. The example of the aligned holes is highlighted and zoom in is shown in figure 4.1.2.2.

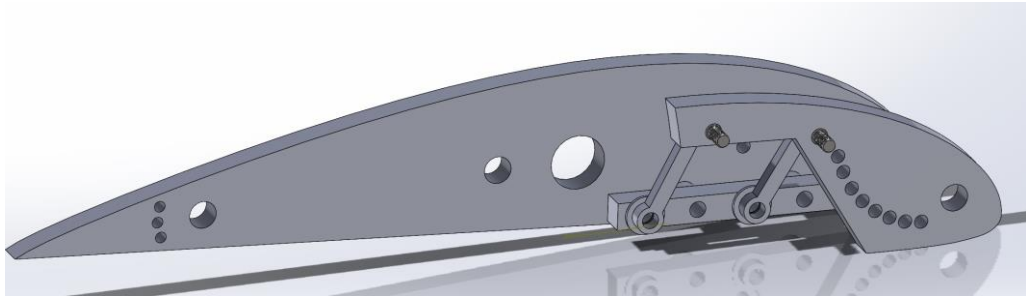


Figure 4.1.2.1: Overview of the CAD model of the slat's mechanism.

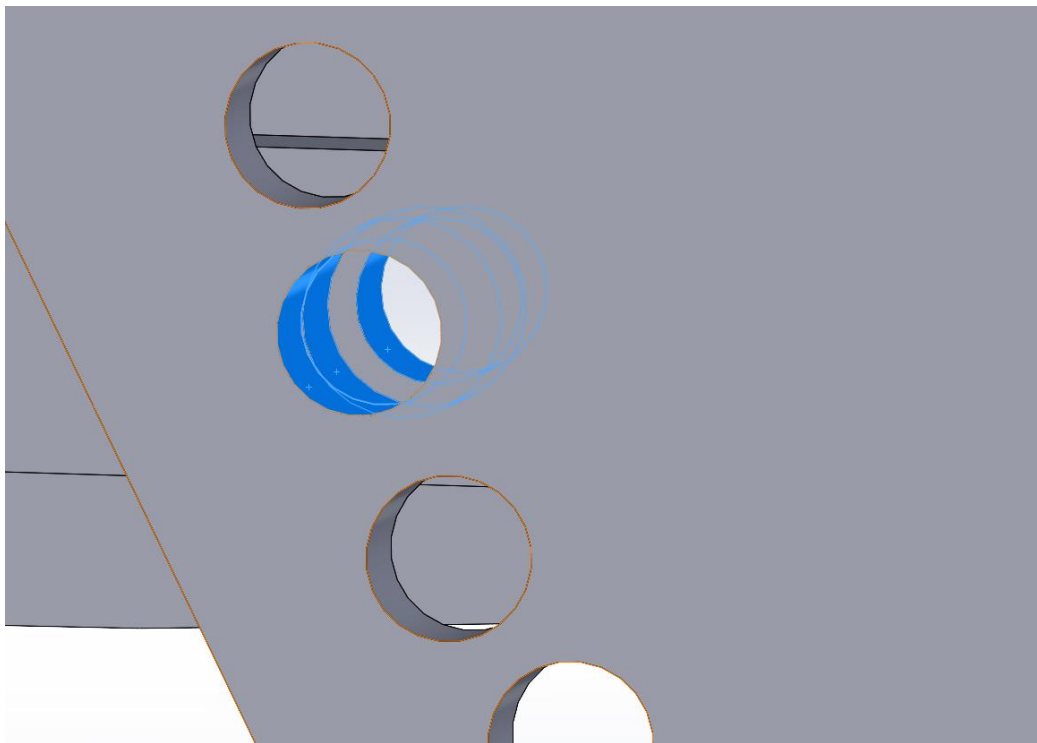


Figure 4.1.2.2: Highlighted Aligned Holes.

The final design of the slat's mechanism consists of 4 parts. A base act as two fix point of the four-bar linkage, two moving bars with the bottom point of them connect to the base, and a unique rib made to connect the body of the slat and with the two-moving bar of the mechanism. The slat's body have chord length of 35% full chord length and expands for 0.034m, which is 10% elongation. The assembled part with fully deflected slat is shown in figure 4.1.2.4.

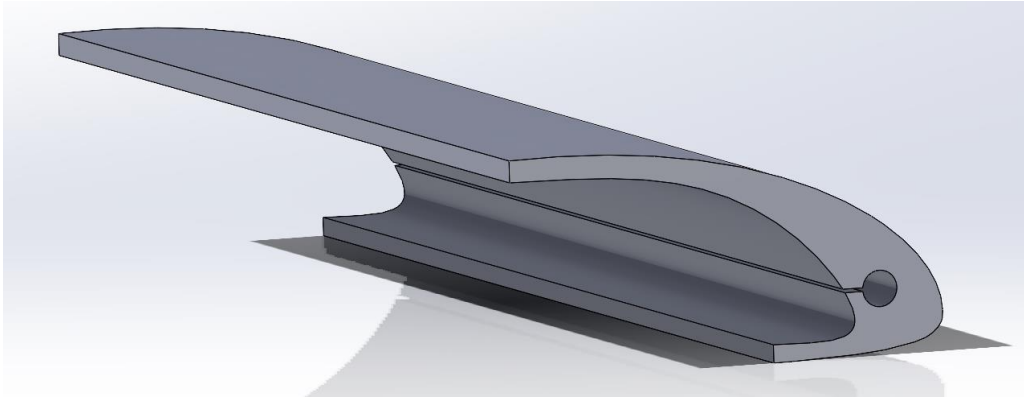


Figure 4.1.2.3: CAD Model of the Slat's Body.

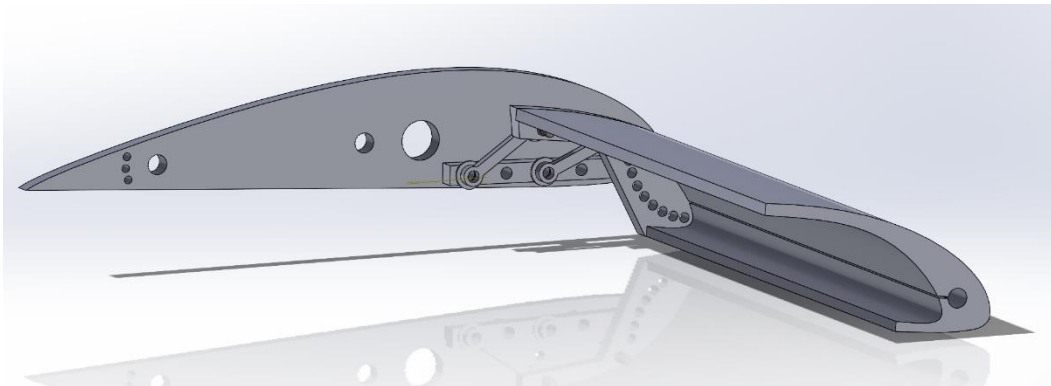


Figure 4.1.2.4: Assembly of the Slat's Mechanism.

#### 4.1.3 Flap's Mechanism

The flap chosen for this project is the plain flaps. It is visualized on figure 3.9(a) on the previous section. The objective of this flaps is to rotate downwards to deform the airfoil into a more positively cambered shape. There should be no gap between the trailing-edge flaps and the body of the wing to forbid any flow from mixing through it. The pivot point of the rotation is located 0.28m from the leading edge. The flaps itself have chord length of 0.1m which is 29.4% of the overall chord length of 0.34m. The upper surface of the flap is trimmed to avoid any protruding part as the flap rotate down. The flap fix in position by using similar method as the slat. Aligning hole on the flap with holes on main rib of the wing and slotting a bar through it will prevent the rotation. The difference will be due to the limited thickness on the flap body, it is advice to only cut one anchoring hole on it. The holes for different positioning are therefore, cut on to the main rib. Figure 4.1.3.1 & 4.1.3.2 shows the flap design.

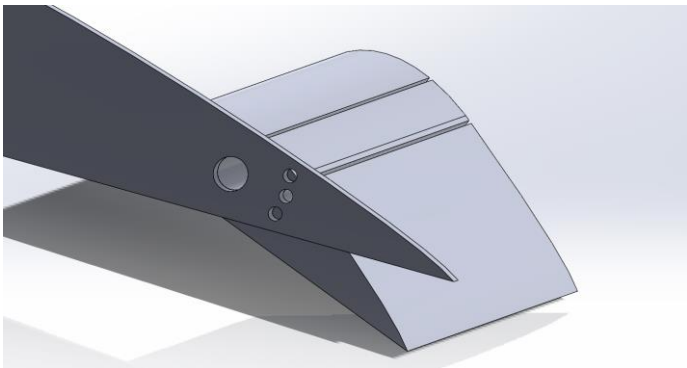


Figure 4.1.3.1: CAD Assembly of the Mechanism of the Flap.

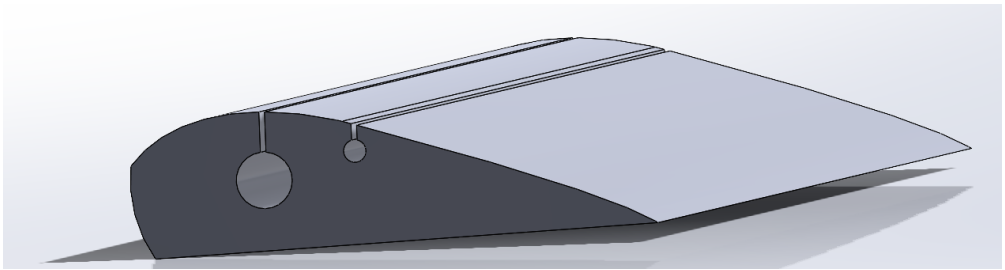


Figure 4.1.3.2: CAD Model for the Flap's Body.

#### 4.1.4 Main Body

Due to the cut out for the high-lit devices, the body for the middle part of the wing will take form of the modified airfoil as shown in figure 4.1.4.1. Some light modification is implied to avoid collision with the mechanism of the slat. The 20mm hole internal feature of this part is made for the main spar of the wing.

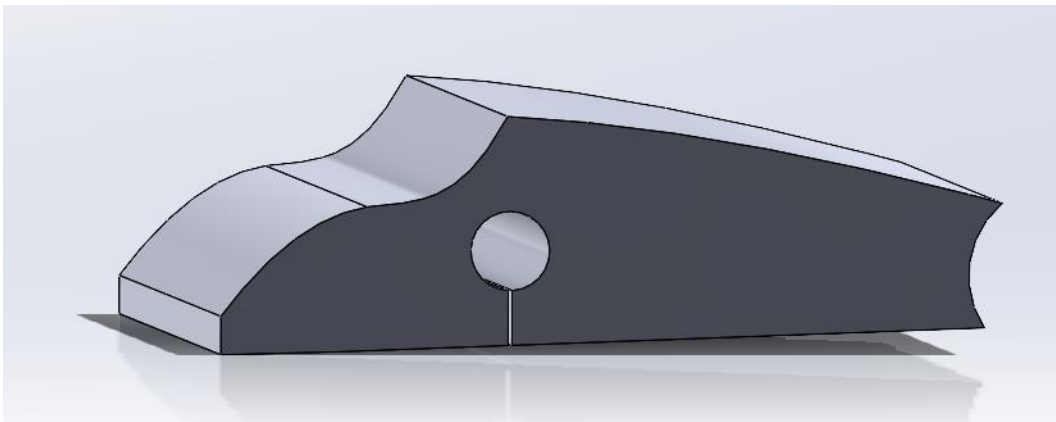


Figure 4.1.4.1: CAD model of the main body of the wing.

The complete cross-sectional look of the wing in its “clean” configuration (meaning no deployment of any high-lift devices) & 100% deployment configuration is shown in figure 4.1.4.2 & 4.1.4.3.

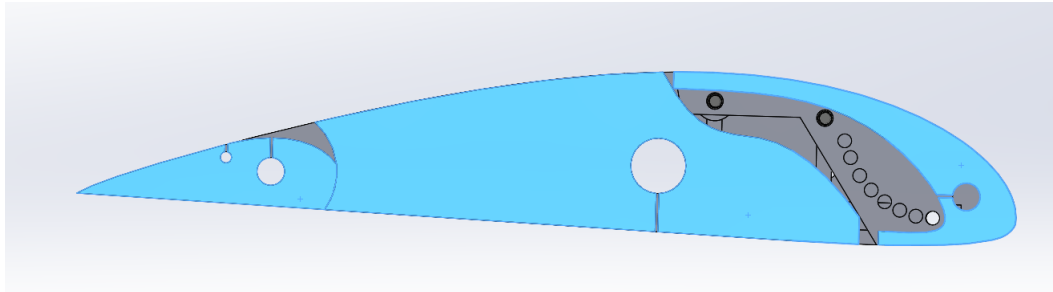


Figure 4.1.4.2: Clean Configuration’s Side View.

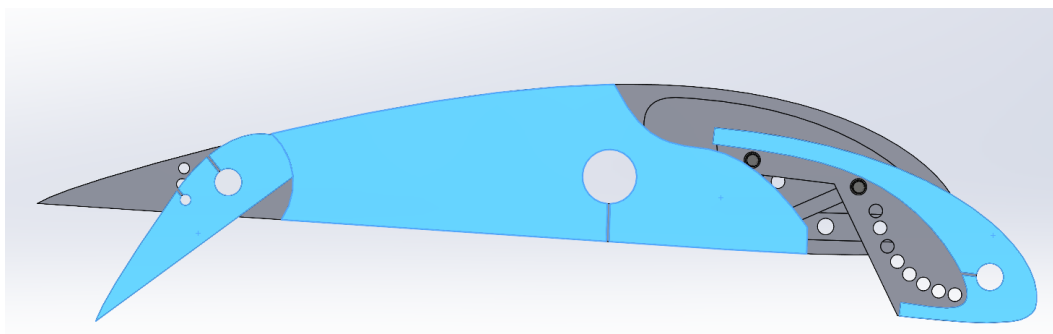


Figure 4.1.4.3: 100% Deployment Configuration’s Side View.

#### 4.1.5 Tapered Body

The wing consists of two different parts, the “rectangular” part which is used to fit in the high-lift devices and the tapered part which will be attached, spanwise, after the rectangular part. The tapered part of the wing has span of 0.6m and tapered ratio of 0.5 as discussed above.

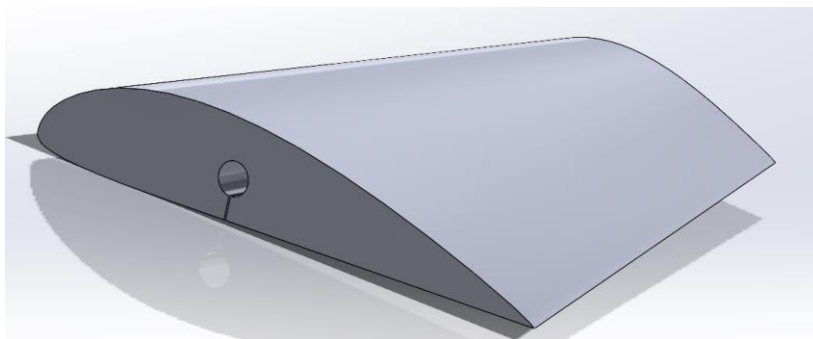


Figure 4.1.5.1: CAD model for the tapered part of the wing

This part is designed such that the quarter-chord point of the root chord and the tip chord are aligned. Similar to the main body above, a 20mm hole is made to fit in the main spar.

#### 4.1.6 Ribs

The ribs of the wing combined with the main spar, held responsibility of holding the wing in position. The connection points of the slat, flap and the main body are all held in place by the ribs. The main internal feature of the rib is the biggest hole ( $D = 20\text{mm}$ ) located 37% of the overall chord length which will fit in the main spar of the wing. The main spar is parallel to the wingspan and goes through all the major bodies along the line to prevent any dislocations. Small holes in the front part of the rib includes mounting point of the slat's mechanism and alignment holes for the mounting mechanism to the wind tunnel. The thickness for the rib is 10mm. Below figure 4.1.6.1 shown an example piece of the rib.

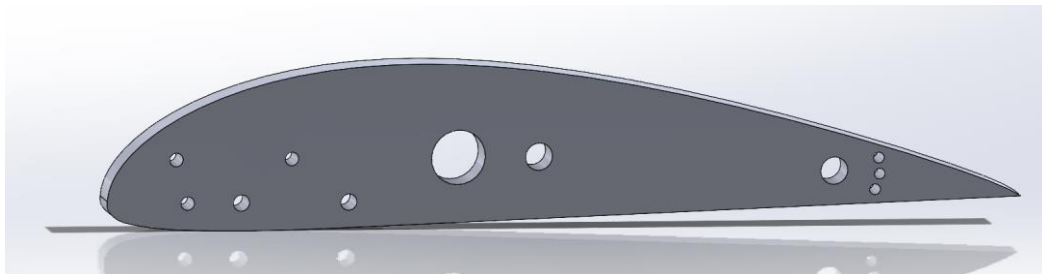


Figure 4.1.6.1: CAD model of the main rib

A smaller version of the rib (figure 4.1.6.2) is also designed for the tip of the tapered part. All unnecessary mounting holes are removed from it as there will be no control surfaces lies on the tapered body. The only hole in the rib, which is 20 mm in diameter is meant for the main spar.



Figure 4.1.6.2: CAD model of a smaller rib (for wingtip)

## 4.2 Manufacture of the Wing

### 4.2.1 Bodies the Wing

The body of the wing includes the slat, flap, and the main & tapered body. These parts will be made of foam to reduce the unnecessary weight for easier transporting and assembly. The designs are slightly modified for the foam cutting machine to work properly. Since the machine only cut in a straight line, a few considerations need to be made as there are shape that are unable to be manufactured. For example, thin surfaces would also cause deformation as the wire is heated. In addition, a thin 1mm width channel is constructed linking the internal features (i.e., the holes for main spar, pivot point for flaps, etc.) to either the upper or lower surface. The channel creates a path for the wire to cut inside the foam. The channel will be tape after the cutting is done to create a close surface (especially important for the upper surface). Sharp points, such as the trailing edge of the wing needs to be fillet with a circle (as shown in the trailing-edge of figure 4.2.1) that can then be easily remove using a blade afterwards. DXF files are used for the machine to cut accordingly. Figure 4.2.1 demonstrated an example of the 2D surface of the flap in DXF files.

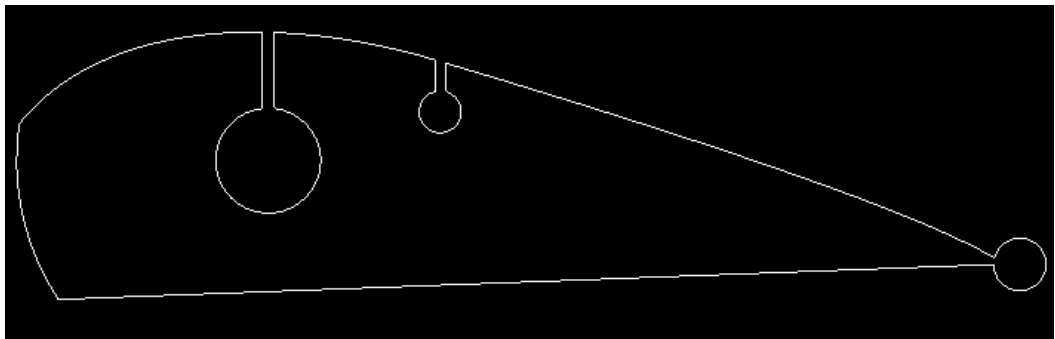


Figure 4.2.1: 2D Shape of The Flap

### 4.2.2 Ribs

All the ribs of the wing will be made from plywood. The plywood is laser cut into the desired shape with all the internal features included. Considering structural strength, at least 10mm thickness is required for every piece of rib. Therefore, with only 5mm plywood available, 2 pieces of identical rib with thickness of 5mm are glued together

using epoxy resin.

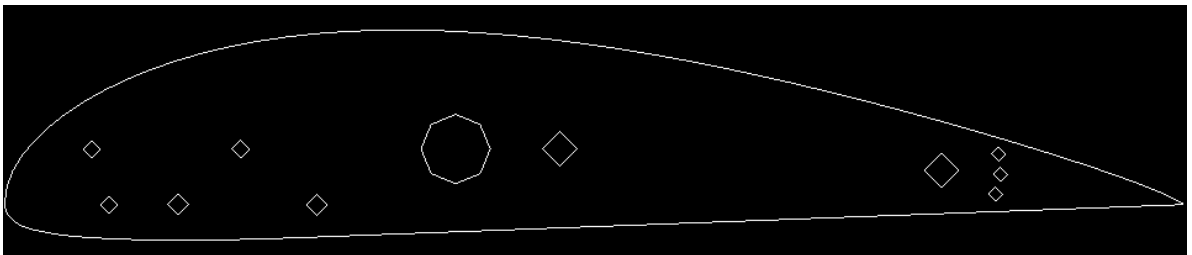


Figure 4.2.2: 2D Shape of the Main Rib

#### 4.2.3 Slats Mechanism

The slat mechanism has a total of 4 separate part. Due to the importance of accuracy and structural strength (the parts are small), stainless steel is chosen to be the material for the parts. The CNC machine is used to manufacture the part accordingly. To compensate the tiny error, the holes are made 0.1mm smaller and can then be hand filed to fit in the bolts.

### 4.3 Mounting of the Wing

The wing is fixed in the wind tunnel force balance by anchoring the main spar of the wing and a few additional fitting components. Figure 4.3.1 & 4.3.2 below shows the components used to compensate the different diameter of the spar with the tube mounted on the force balance of the wind tunnel.



Figure 4.3.1: Steel Mount



(a) Wooden Fitting Component

(b) Steel Mount & Wooden Component

Figure 4.3.2: Fitting Component.

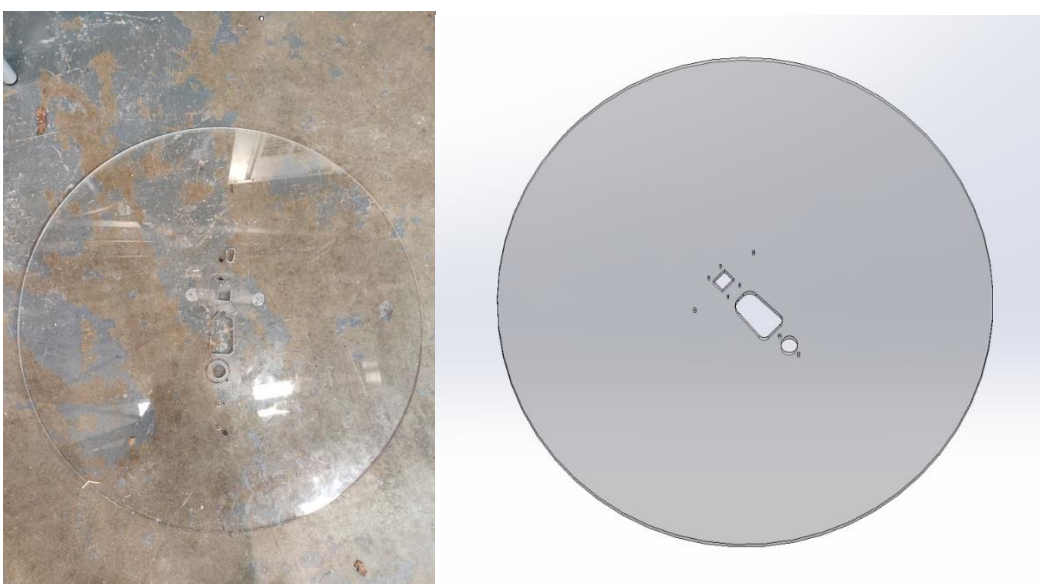


Figure 4.3.3: Acrylic Splitter

The spar and the component are fixed to the force balance by having a 6mm diameter hole drilled through them that align with the steel mount. To provide the wing with a clean flow, a flat (thickness of 5mm) acrylic circle plate (Figure 4.3.3) is placed in between the mounting part and the wing itself. To prevent the plate from rotating, two anchoring holes are drill on the plate matching the two holes on the ribs of the wing. Two aluminium pin is fitted through them, and the circular motion of the splitter is successfully neglected. The wing is then set to zero angle of attack by aligning its bottom flat surface using a laser device. The offset for the wind tunnel is then recorded.

#### 4.4 Process of the Testing

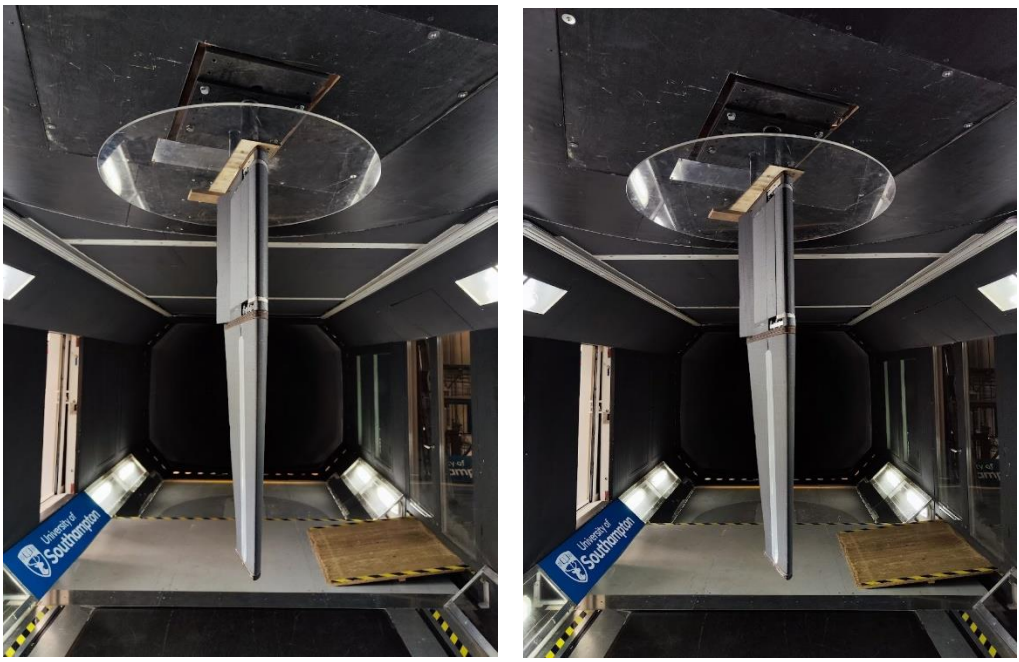
After setting up the wing, the test began from  $-4^\circ$  angle of attack, increment by  $2^\circ$  until  $15^\circ$ . The increment is then reduced to  $1^\circ$  for a more precise data at the near stall angle. The angle of attack of the wing varies using the turnable coordinate system of the wind tunnel which rotates the wing around the vertical axis. The test was repeated in different configurations of the high lift devices. Starting off with no deployment, then 50% deployment of both and then 100% deployment. Most tests are conducted in 10m/s of wind speed and there are some alternatives conducted in 15m/s. The wing must be removed from the force balance to swap the configurations. Therefore, it is essential to check the alignment for the zero angle of attack and record down the angle offset for further calculations.



(a)  $0^\circ$  AoA



(b)  $10^\circ$  AoA



(c)  $15^\circ$  AoA

(d)  $20^\circ$  AoA

Figure 4.4.1: Front View of Wing on Different Angle of Attack (50% Flaps 0% Slats).

## 4.5 Processing & Calculations of Wind Tunnel Data

The data obtained from the wind tunnel follows the following table 4.5.1 format.

Comment	Lift(N)	Side(N)	Drag(N)	Roll(N m)	Wind_m/s	DynPx_mm H2O	T_oC	AmbPx_mb
U00m/s	0.02 8	0.016	0.003	-0.01	0	0	14.9 64	989.168

Table 4.5.1: Sample Data from Collected from the wind tunnel.

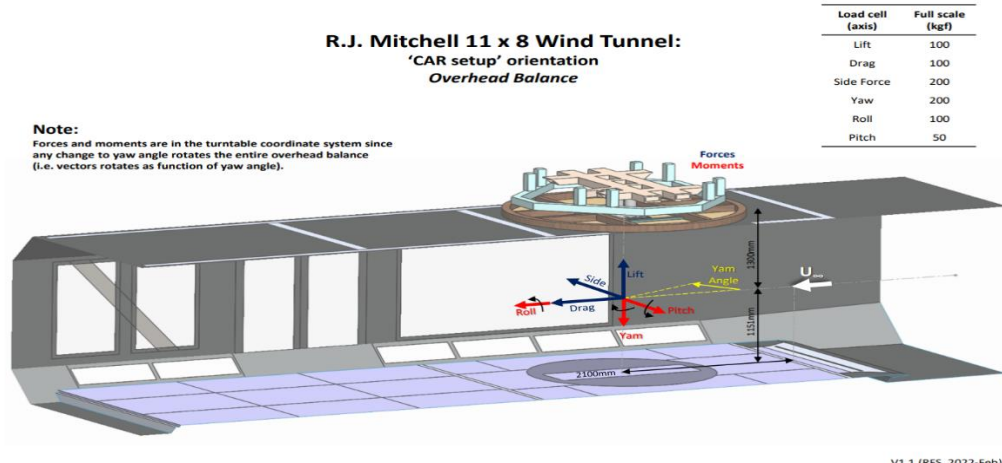


Figure 4.5.1: Mitchell Wind Tunnel Balance Schematic.

To calculate the lift and drag of the wing, the side and drag force are the main readings that need to be considered. The operations of the turnable coordinate system does rotate the force balance of the wind tunnel as well. Therefore, further process of the force report is needed. Figure 4.5.1 shows the wind tunnel force balance schematic. Since the wing is setup vertically in the test section, the side & drag force measured by the balance both contributes to the actual lift and drag force generated by the wing.

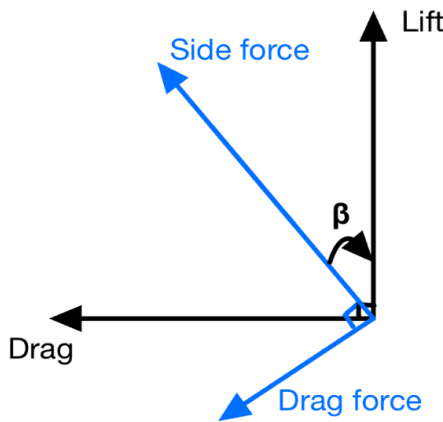


Figure 4.5.2: Force Diagram

The side and drag force that are measured by the force balance is highlighted in blue while the generated lift and drag force of the wing is black as shown in figure 4.5.2. It is obvious that the measured side and drag force will contributes to both the actual lift and drag.  $\beta$  is the angle between the side force and actual lift and will be equal to the angle between drag force and actual drag.

$$\beta = \alpha + \gamma \quad (1)$$

$\beta$  is the addition of the angle of attack,  $\alpha$  and the offset angle,  $\gamma$ . The force measured can then be converted to the actual lift and drag using equations 2, 3 & 4.

$$L_s = F_s \cos(\beta) , D_s = F_s \sin(\beta) \quad (2)$$

$$L_d = F_d \sin(180^\circ - 90^\circ - \beta) , D_d = F_d \cos(\beta) \quad (3)$$

$$L = L_s + L_d , D = D_s + D_d \quad (4)$$

$L_s$  &  $D_s$  represents the side force induced lift and drag, the  $L_d$  &  $D_d$  represents the drag force induced lift and drag. The sum of the induced lift will be the actual total lift. Same goes for the total drag.

To further reduce the error, a clean test without the wing and just the mounting components are also conducted. The force generated are process using the same

method as above. This is to be subtracted from the total lift & drag to obtain the clean forces generated by the wing itself.

The density is calculated using the temperature and pressure given from the wind tunnel data (Table 4.5.1). By using the ideal gas law (Equation 5),

$$P = \rho RT \quad (5)$$

P is the pressure in Pascal,  $\rho$  as density in  $\text{kg/m}^3$ , R is the gas constant and T as temperature in Kelvin. Taking account that the data recorded in the tunnel according to table, the numbers are in mbar for pressure and degree Celsius for temperature, the ideal gas equation is modified and rearrange as equation 6.

$$\rho = \frac{100P}{R(T+273.15)} \quad (6)$$

Where R will be taken as  $287\text{J/kgK}$ . The lift and drag coefficient are then calculated using equation 7 & 8 as follow.

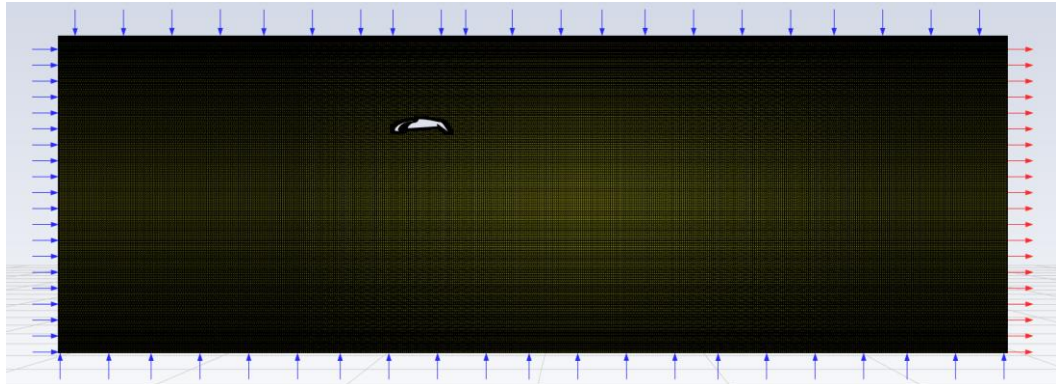
$$C_L = \frac{L}{0.5\rho V^2 S} \quad (7)$$

$$C_D = \frac{D}{0.5\rho V^2 S} \quad (8)$$

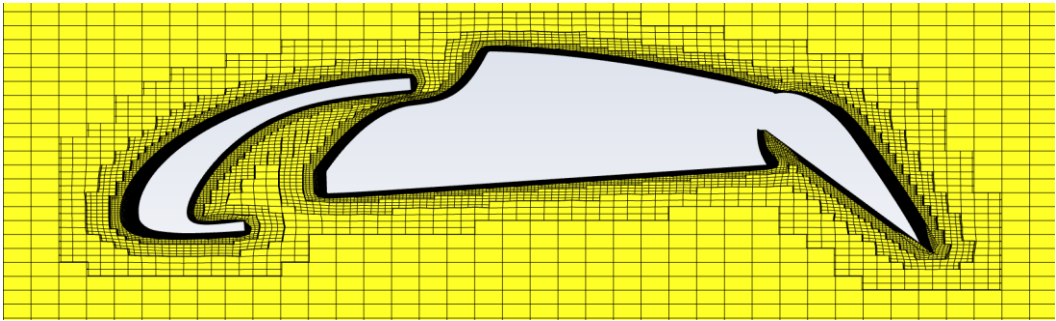
With  $C_L$  as lift coefficient and  $C_D$  as drag coefficient, V as the wind speed of the wind tunnel in  $\text{ms}^{-1}$  and S as the references area of the wing.

## 4.6 CFD Methods

The mesh created for the CFD results for predicting the forces of the airfoil are constructed using Harpoon. The zoomed in mesh is visualized in figure 4.6.1(b).



(a) Full Domain of the Mesh.



(b) Mesh of Airfoil on Full Deployment (Zoomed In).

Figure 4.6.1(a)(b): Mesh Created Using Harpoon.

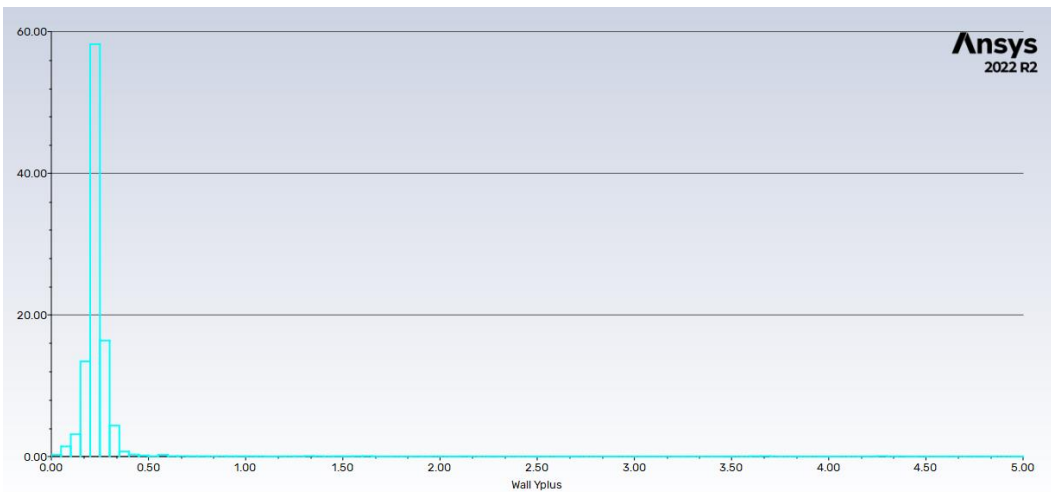


Figure 4.6.2: Wall Yplus of the Mesh.

Domain Extends								
Xmin (m)	Xmax (m)	Ymin (m)	Ymax (m)	Zmin (m)	Zmax (m)	X Distance (m)	Y Distance (m)	Z Distance (m)
-2	4	-1	1	0	0.025	6	2	0.025

Table 4.6.1: Domain of Mesh.

Table 4.6.1 shows the domain extensions of the following mesh. The wing itself have chord length of 0.34m, positioned on the centre of the x, y & z axis. The mesh contains 1184505 total cells with minimum orthogonality of 6.63508e-02 and maximum aspect ratio of 1.43554e+02. Figure 4.6.2 shows the histogram of wall yplus plotted in 100 division. Normally, it is preferring to have the wall yplus below 1 in order to better mimic the flow around the high lift devices. Since the majority of cells are under the value of 0.5, the requirement is fulfilled.

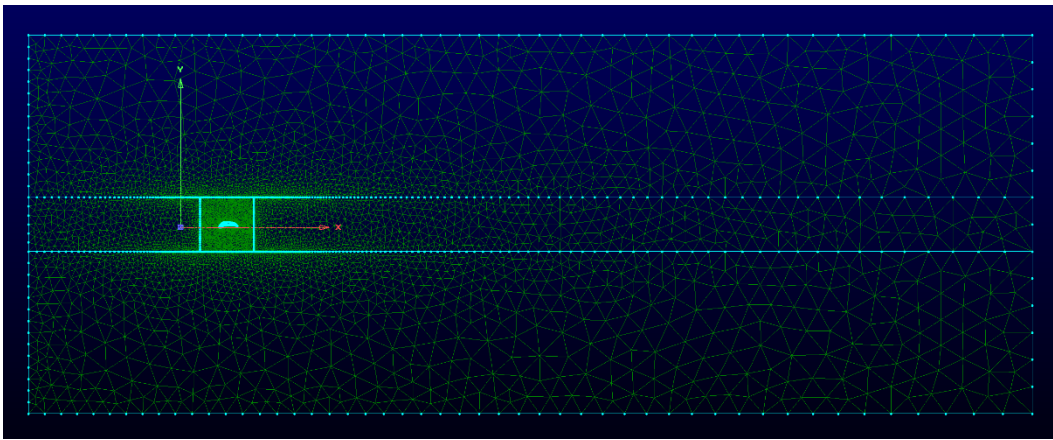
Due to the high complexity of flow around the high lift devices, a transient approach is carried out in order for a higher accuracy result. The solver type is set to pressure based as the simulation flow speed compensate the wind tunnel testing of 10m/s. The

viscous modelling for initial convergence is chosen to be the S-A (Spalart-Allmaras) method from the Ansys Fluent RANS (Reynolds-Averaged Navier-Stokes) family for quicker convergence while providing sufficient condition for the calculations afterwards. To avoid the convergence criteria being limited to the pressure-velocity coupling in this initial step, SIMPLEC (Semi-Implicit method for Pressure-Linked Equations – Consistent) scheme is prefer over SIMPLE despite the similar convergence rates. To compensate the time for transient solver, the pressure discretization is set to standard, momentum & turbulent viscosity are set to first order upwind. Pseudo time method is set to local time step and first order implicit for transient formulation. This setting runs for a 1000 time steps with 0.01 step size with 30 iterations/time step.

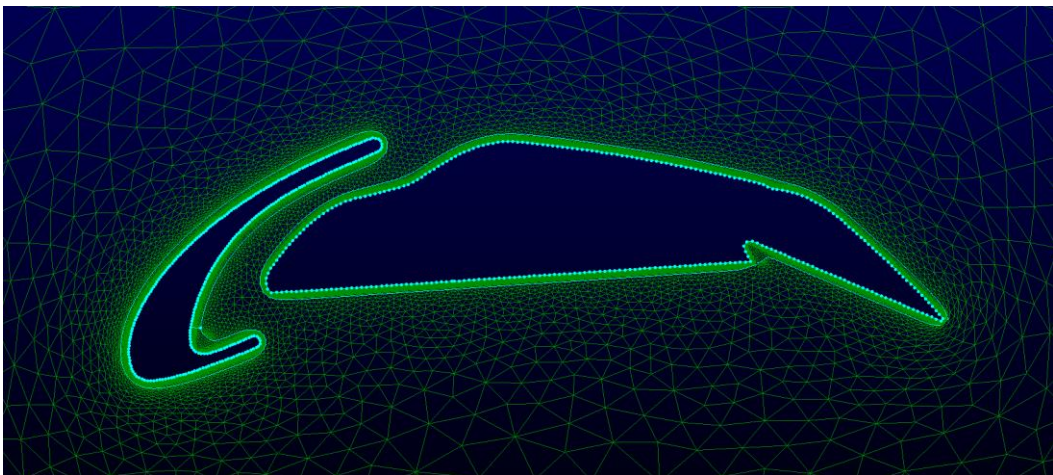
The continuity after the initial step should reaches value below 1e-6. The viscous modeling is then switch to a more intense model of k- $\omega$  SST (Shear-Stress Transport) model. The k- $\omega$  SST still does belongs to the RANS family but provides a more precise capture of turbulent flow conditions as all the effects of turbulence are modeled. Briefly speaking the different over the SST model over the standard model in the k- $\omega$  branch, it consists of a more gradual change from the standard model in the inner region of the boundary layer to a high Reynolds-number version in the outer part of the boundary layer. The turbulent shear stress is account for the transport effects in the SST model by modifying the turbulent viscosity formulation. Due to the method of this model, the “low-Re correction” option is enabled for the following test. The pressure-velocity coupling is then switch to PISO (Pressure Implicit with Splitting of Operation) that is commonly used by transient cases. The pressure, momentum, turbulent kinetic energy, and the specific dissipation rate are then all swap to second order upwind for a more precise prediction of the flow.

Additional sets of mesh are created using the Fidelity PointWise software. This mesh is constructed in a simpler and faster way, aimed only for visualizing the approximation of flow around the airfoil and neglecting its inaccurate force reports. An example of the mesh is shown in below figure 4.6.3. (This mesh is used for [figure 6.3.4](#) down at discussion part).

A thin layer of structure mesh with initial cell height of 0.00002986m and growth rate of 1.1 are generated 20 times to provide better prediction of the flow in the boundary layer are first generated. The domain is then filled with auto-generated unstructured mesh. Figure 4.6.4 shows the histogram of wall yplus plotted in 100 division, the majority of the cells wall yplus of the current mesh are below 1.



(a) Full Domain of the Mesh.



(b) Zoomed in Airfoil.

Figure 4.6.3: Mesh Created using Fidelity Pointwise.

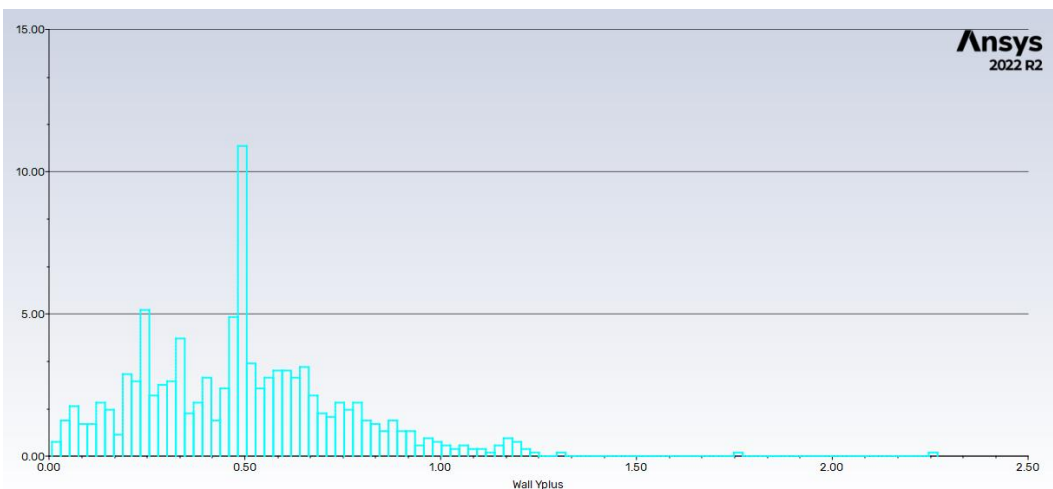


Figure 4.6.4: Histogram of Wall Yplus of the Mesh.

Domain Extends					
Xmin (m)	Xmax (m)	Ymin (m)	Ymax (m)	X Distance (m)	Y Distance (m)
-2.77	15.84	-3.37	3.63	18.61	7

Table 4.6.2: Domain of Mesh.

## **5. Results**

### **5.0 Configurations & Terms**

Below shown the cross-section view of different configuration of the high-lift devices deployment that is used in the testing and the below results are based on these configurations. Since the wing is glued together, it is impossible to show the real wing's cross section, thus a CAD view is used. Clarification regarding the term will be used including, slat meaning the leading edge high lift device and flap being the trailing edge high lift device, stating high lift devices includes both of them.

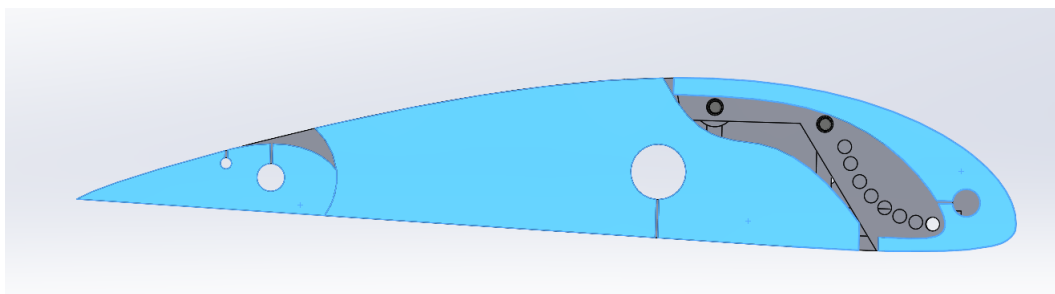


Figure 5.0.1: Clean Configuration. ([5.1 Main Results](#))

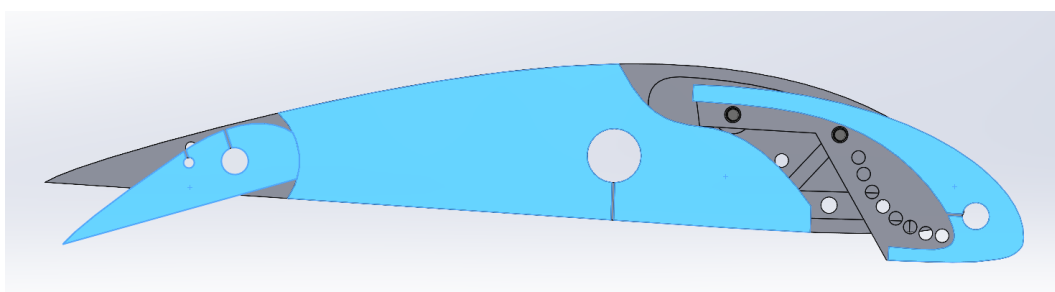


Figure 5.0.2: 50% Slat & Flap Deployment Configuration. ([5.1 Main Results](#))

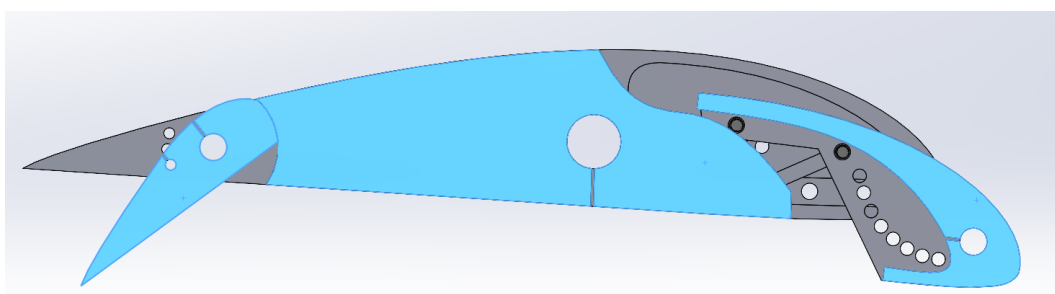


Figure 5.0.3: 100% Slat & Flap Deployed Configuration. ([5.1 Main Results](#))

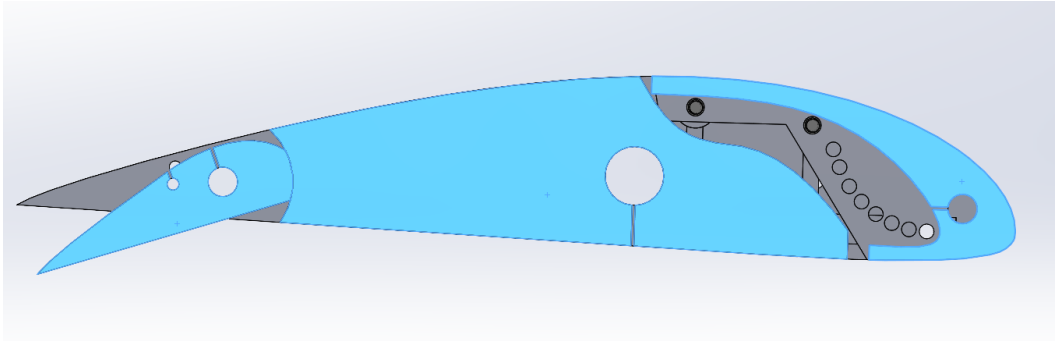


Figure 5.0.4: 0% Slat 50% Flap Deployed Configuration. ([5.2 Individual Testing for Trailing-Edge Flaps](#))

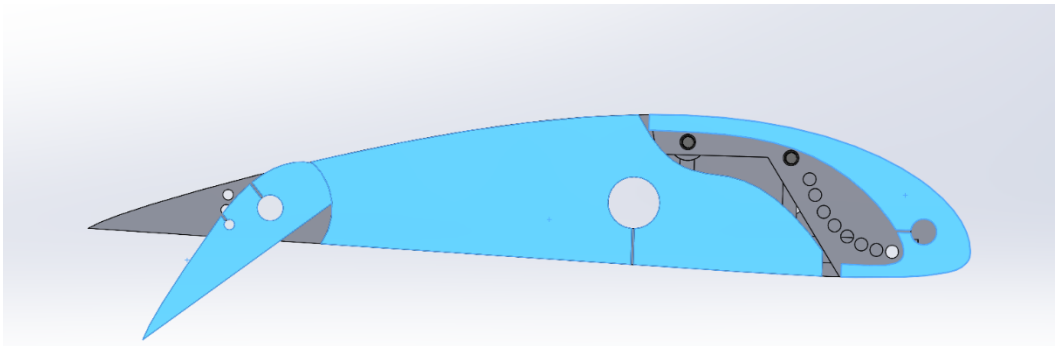


Figure 5.0.5: 0% Slat 100% Flap Deployed Configuration. ([5.2 Individual Testing for Trailing-Edge Flaps](#))

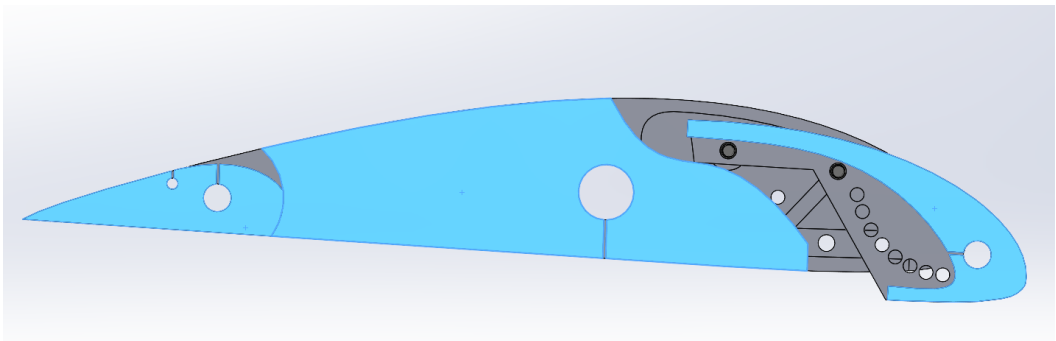


Figure 5.0.6: 50% Slat 0% Flap Deployed Configuration. ([5.3 Individual Testing for Leading-Edge Slats](#))

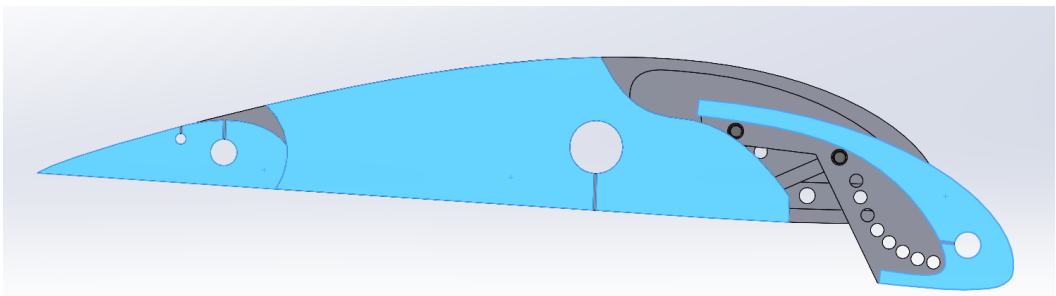


Figure 5.0.7: 100% Slat 0% Flap Deployed Configuration. ([5.3 Individual Testing for Leading-Edge Slats](#))

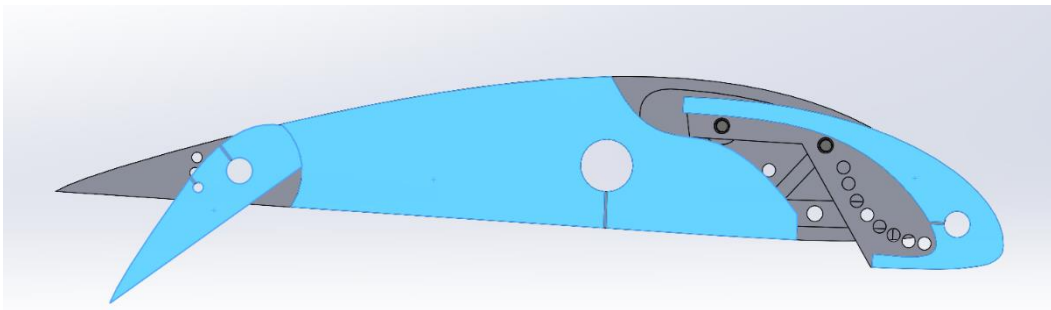


Figure 5.0.8: 50% Slat 100% Flap Deployed Configuration. ([5.4 Special Combination of Deployment of the High Lift Devices](#))

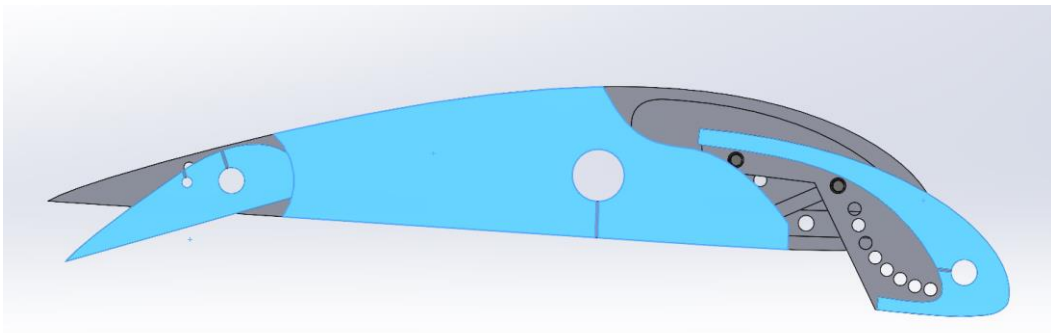


Figure 5.0.9: 100% Slat 50% Flap Deployed Configuration. ([5.4 Special Combination of Deployment of the High Lift Devices](#))

## 5.1 Main Results

After collecting the data from the wind tunnel, calculations are done using Excel and the following lift-curve slope plotted. Clean (Figure 5.0.1), 50% Deployment of High Lift Devices (Figure 5.0.2), 100% Deployment of High Lift Devices (Figure 5.0.3) visualisations can be found in [section 5.0](#).

Angle of Attack	Cl (Clean)	Cl (50%)	Cl (100%)
-4	0.241	-0.003	0.127
-2	0.364	0.149	0.180
0	0.513	0.390	0.384
2	0.637	0.534	0.778
4	0.735	0.648	0.877
6	0.856	0.797	0.982
8	0.952	0.955	1.057
10	1.036	1.044	1.140
12	1.101	1.105	1.207
14	1.149	1.175	1.269
15	1.167	1.204	1.290
16	1.189	1.210	1.302

17	1.208	1.228	1.326
18	1.214	1.245	1.336
19	1.225	1.262	1.344
20	1.218	1.270	1.339
21	1.210	1.268	1.328
22	1.198	1.266	1.320

Table 5.1.1: The Lift Coefficient of Various Configuration of the High Lift Devices.

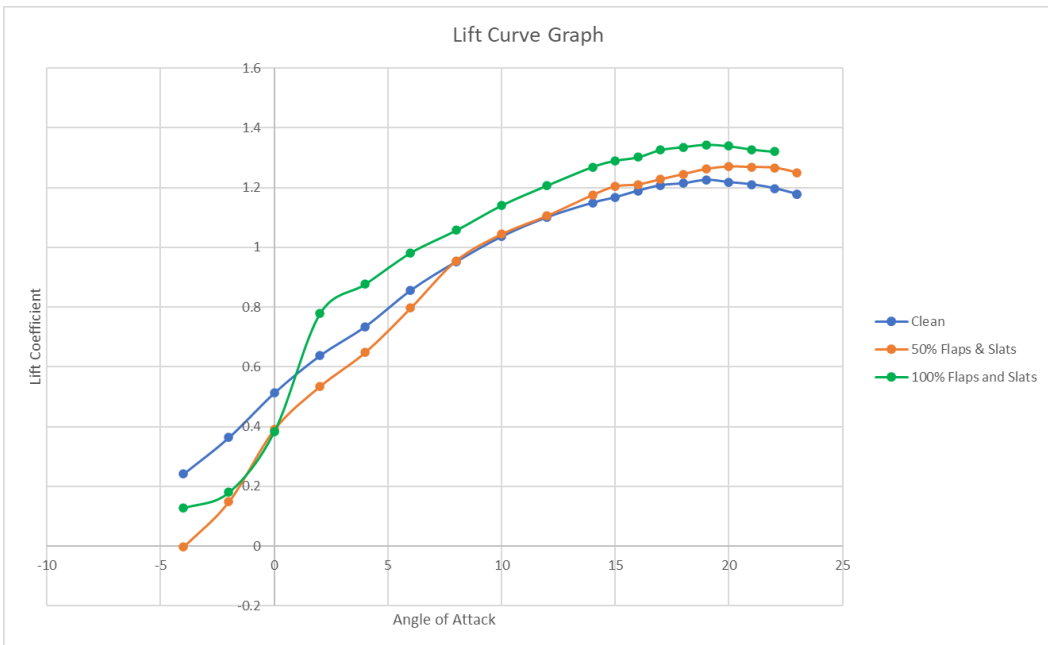


Figure 5.1.1: Lift-Curve Graph of Various Configurations of the High Lift Devices.

The table 5.1.1 and figure 5.1.1 show the lift coefficient and the lift curve slope for no deployment of any high lift device(clean), 50% deployment (50%) and 100% deployment (100%) of the high lift devices on the wing. Referring the figure, the clean wing with no deployment reaches it's  $C_{LMax}$  of 1.225 at angle of attack of 19°. Referring table, the fully deployed (100%) flaps and slats starts to increase the  $C_L$  from 2° of angle of attack. Reaching  $C_{LMax}$  of 1.344 at 19°, which is 9.71% higher than the  $C_{LMax}$  of the clean wing.

The 50% deployment configuration achieved it's  $C_{LMax}$  of 1.27 at 20° angle of attack, 3.67% higher than the  $C_{LMax}$  of the clean wing configuration. The increase in  $C_L$  for this configuration only take place after 8° angle of attack, referring to table 5.1.1 and figure 5.1.1.

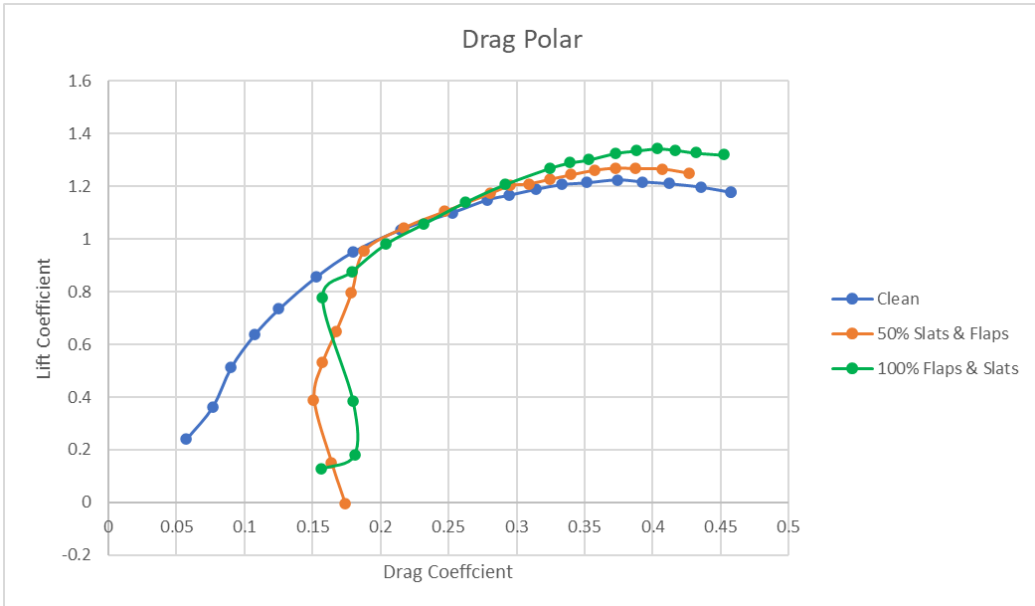


Figure 5.1.2: Drag Polar of Various Configurations of the High Lift Devices.

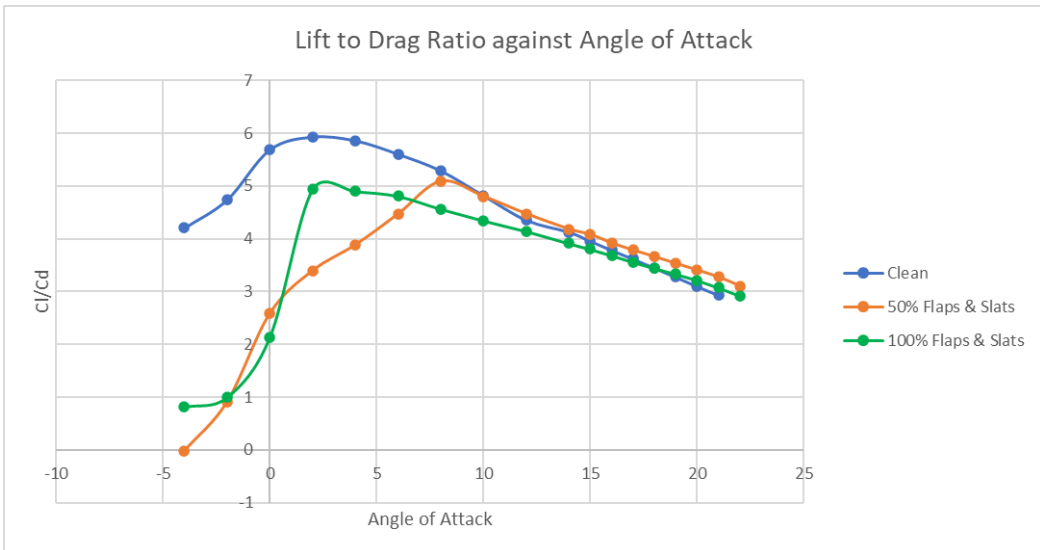


Figure 5.1.3: L/D ratio against Angle of Attack.

Referring to figure 5.1.2, the drag penalty after extending the high lift devices is significant at low angle of attack. The outcome of the drag is also reflected on figure 5.1.3. The lift to drag ratio of the half-deployed and fully deployed cases peak around 5 while the clean wing reaches 6. To understand regarding the drag contribution of each piece of high lift device, it is needed to conduct individual test of them.

## 5.2 Individual Testing for Trailing-Edge Flaps

A few additional tests are conducted to understand the contribution of each piece of the high lift device toward the lift & drag. Table 5.2.1 and figure 5.2.1 below are test

results of lift coefficient varying the trailing edge flaps while keeping the leading-edge slats undeployed. Figures 5.0.4 & 5.0.5 in [section 5.0](#) visualize the cross section of the deployment state.

Angle of Attack	CI (Clean)	CI (50%Flaps)	CI (100%Flaps)
-4	0.241	0.508	0.573
-2	0.364	0.641	0.703
0	0.513	0.778	0.865
2	0.637	0.889	0.974
4	0.735	0.995	1.069
6	0.856	1.118	1.168
8	0.952	1.172	1.252
10	1.036	1.221	1.297
12	1.101	1.273	1.331
14	1.149	1.297	1.380
15	1.167	1.321	1.392
16	1.189	1.331	1.394
17	1.208	1.332	1.408
19	1.214	1.318	1.371
20	1.225	1.310	1.361
21	1.218	1.289	1.356
22	1.210	1.258	1.335

Table 5.2.1: Lift Coefficient of Different Flaps Configurations.

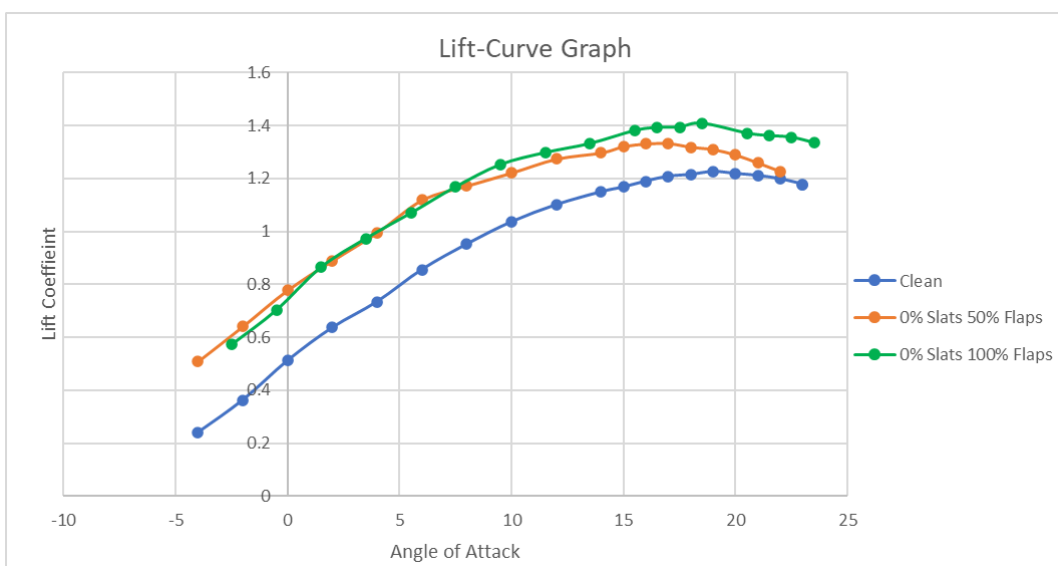


Figure 5.2.1: Lift-Curve Graph of Various Deployment of the Flaps.

Table 5.2.1 compared the lift coefficient of the clean wing and different deployment of the trailing edge flaps without any extension of leading-edge slats. The results shows that the flaps do increase the  $C_{LMax}$  of the wing. The  $C_{LMax}$  is reached at  $17^\circ$  angle of attack for both the 50% and 100% extended flaps configuration. The increase in  $C_{LMax}$  are 8.73% and 14.94% respectively. Figure 5.2.1 have demonstrated that the overall  $C_L$  of the 50% and 100% flaps deployment configuration have high similarity lift-curve graph. Both reached it's  $C_{LMax}$  quicker with respect to angle of attack, causing the wing to stall earlier.

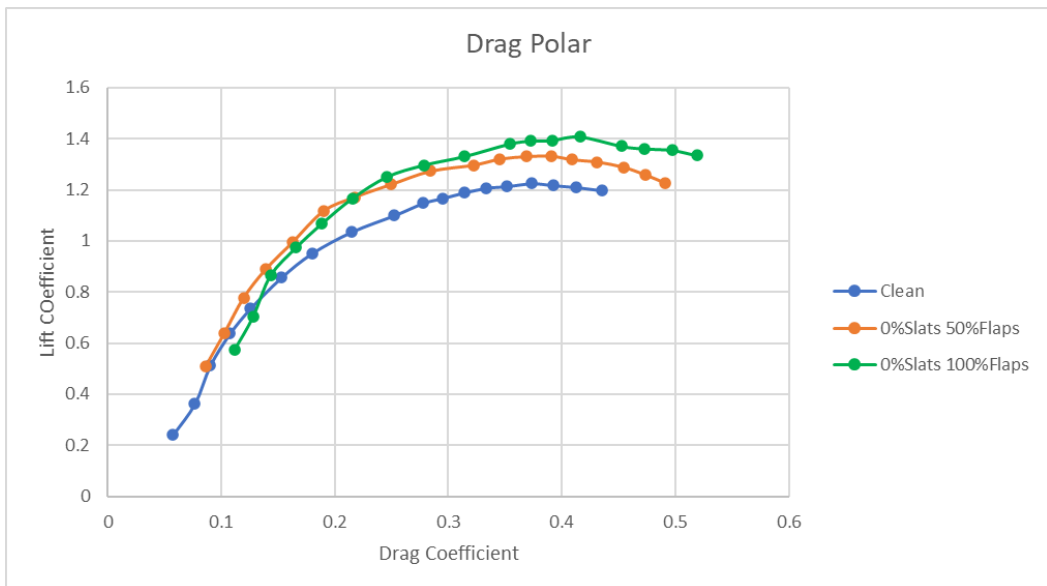


Figure 5.2.2: Drag Polar of Different Flaps Configurations.

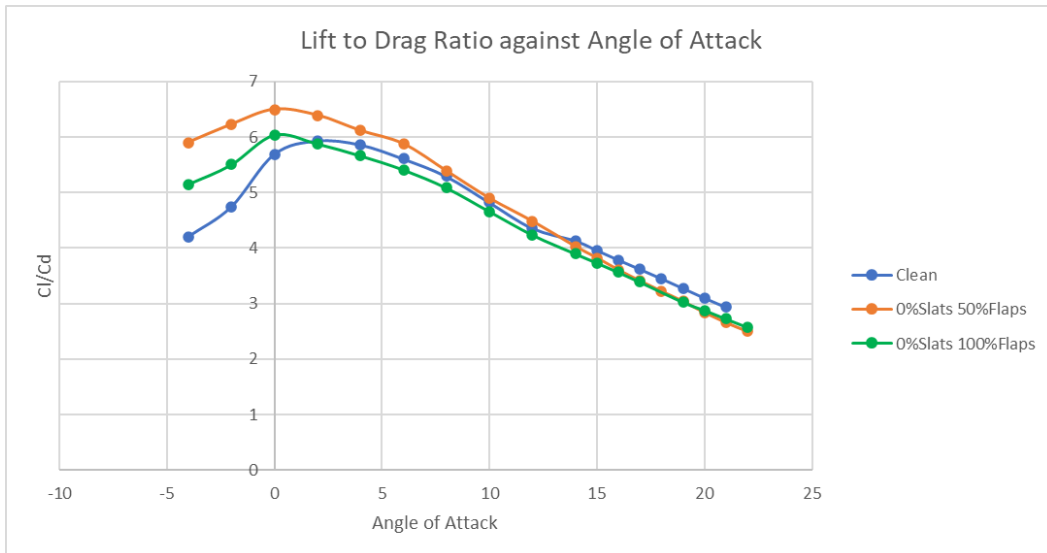


Figure 5.2.3: L/D ratio against Angle of Attack.

Figure 5.2.2 shows the curve of the orange and green line started and ended on a higher drag coefficient than the blue line. This represents that the amount of drag

produce after deploying the flaps are increased. For the fully extended flaps case, the lift to drag ratio (Figure 5.2.3) has dropped below the clean wing at  $2^\circ$  angle of attack. While for the half-extended case, the ratio remains above the clean wing until it reaches  $12^\circ$  angle of attack. Still, the general curve of the ratio is similar.

### 5.3 Individual Testing for Leading-Edge Slats

The following table 5.3.1 and figure 5.3.1 show the result of various deployment of the leading-edge slats and keeping the trailing edge flaps undeployed. Figures 5.0.6 & 5.0.7 in [section 5.0](#) visualize the cross section of the deployment state.

Angle of Attack	Cl (Clean)	Cl (50%Slats)	Cl (100%Slats)
-4	0.241	0.323	0.181
-2	0.364	0.416	0.224
0	0.513	0.530	0.365
2	0.637	0.635	0.483
4	0.735	0.747	0.655
6	0.856	0.835	0.749
8	0.952	0.920	0.828
10	1.036	0.993	0.914
12	1.101	1.048	0.980
14	1.149	1.093	1.002
15	1.167	1.138	1.038
16	1.189	1.140	1.048
17	1.208	1.141	1.048
19	1.225	1.129	1.050
20	1.218	1.117	1.053
21	1.210	1.111	1.041
22	1.198	1.096	1.027

Table 5.3.1: Lift Coefficient of Different Slats Configurations.

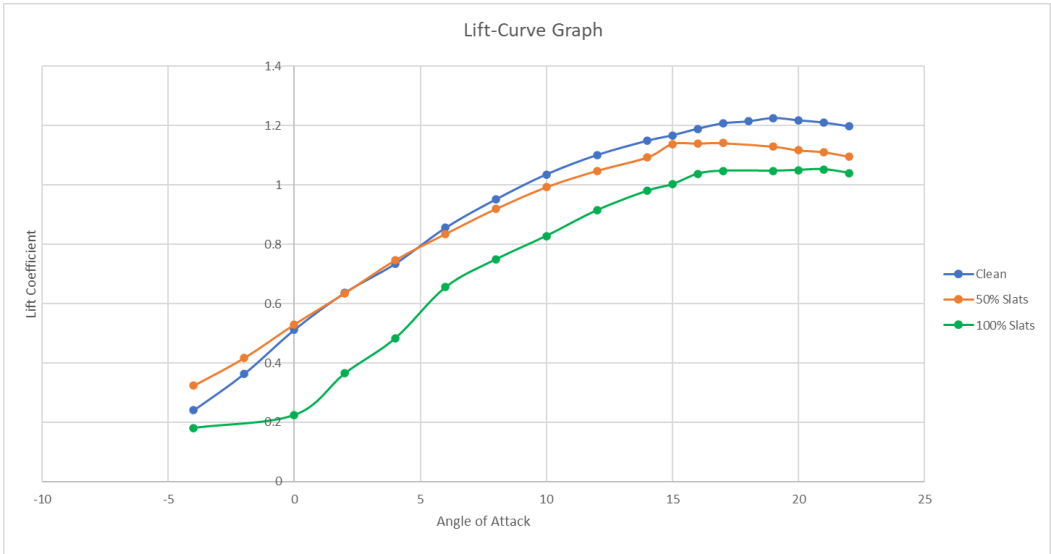


Figure 5.3.1: Lift-Curve Graph of Various Deployment of the Slats.

The table 5.3.1 have shown that the deployment of the slats effectively decreases the lift coefficient of the wing. The  $C_{LMax}$  of the 50% & 100% leading edge slats deployment configuration has decrease by 6.86% and 14.04% respectively.

The fully deployed slats reach it  $C_{LMax}$  at  $20^\circ$  angle of attack.

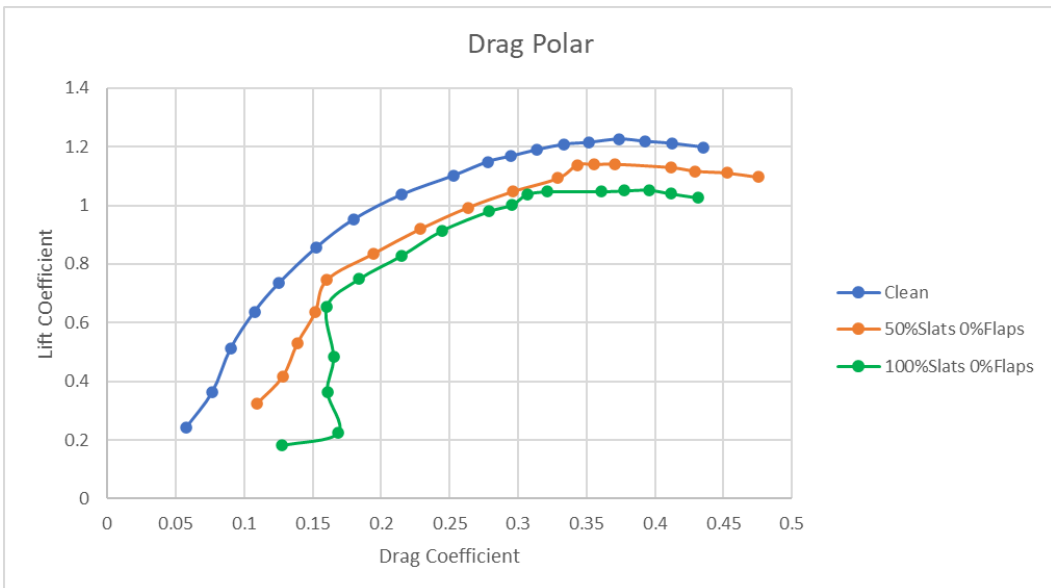


Figure 5.3.2: Drag Polar of Different Slats Configurations.

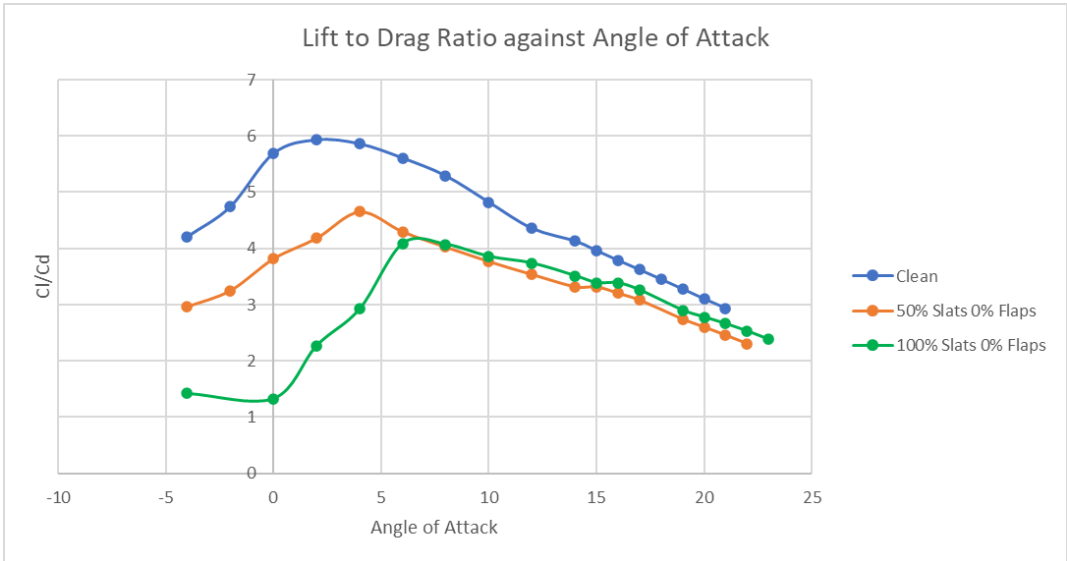


Figure 5.3.3: L/D ratio against Angle of Attack.

Figure 5.3.2 shows that the overall drag after deploying the slats has increased compared to the clean wing. Due to the addition in drag as well as the reduction in lift, the lift to drag ratio of the slat's extended cases are lower as visualize in Figure 5.3.3.

#### 5.4 Special Combination of Deployment of the High Lift Devices

Below are result from special cases after investigating more into the effect of the combinations of flaps and slats. Figures 5.0.8 & 5.0.9 in [section 5.0](#) visualize the cross section of the deployment state.

Angle of Attack	Cl (Clean)	Cl (50%Slats 100% Flaps)	Cl (100% Slats 50% Flaps)
-4	0.241	0.580	0.072
-2	0.364	0.706	0.235
0	0.513	0.830	0.434
2	0.637	0.883	0.704
4	0.735	0.968	0.813
6	0.856	1.056	0.922
8	0.952	1.125	1.003
10	1.036	1.196	1.096
12	1.101	1.246	1.165
14	1.149	1.294	1.216
15	1.167	1.316	1.237

16	1.189	1.334	1.255
17	1.208	1.347	1.274
18	1.214	1.348	1.275
19	1.225	1.339	1.276
20	1.218	1.334	1.270
21	1.210	1.313	1.263
22	1.198	1.304	1.247

Table 5.4.1: Lift Coefficient of Specials Configurations of the High Lift Devices.

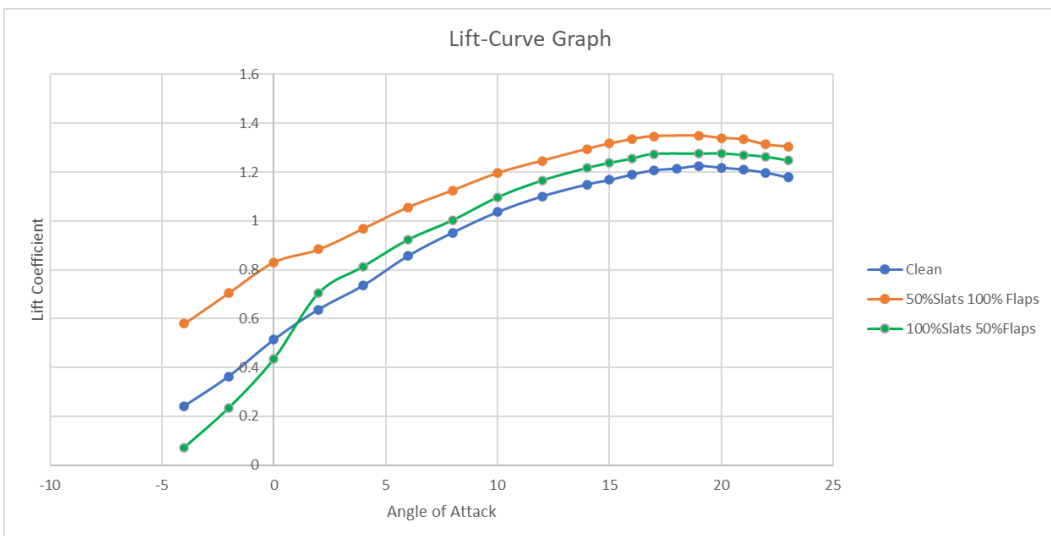


Figure 5.4.1: Lift-Curve Graph of Specials Configurations of the High Lift Devices.

Figure 5.4.1 agree with the individual test result of the slats and flaps. By deploying half of the leading-edge slats and full of the trailing-edge flaps (50%Slats 100% Flaps), the  $C_{LMax}$  is increased to 1.348 at 18° angle of attack, provides 10.04% increase in  $C_{LMax}$  comparing to the clean wing. This configuration has even higher  $C_{LMax}$  than the case with fully deployed slats and flaps ( $C_{LMax}$  of 1.344, referring to table), but also stalling earlier.

The other way around configuration (100% Slats 50% Flaps), also provides increase in  $C_{LMax}$ . The increment is 4.16% and reaches at the same angle of attack as the clean wing.

## 5.5 CFD Results

The CFD are used in predicting the forces at the crucial angle of attack after deploying the high-lift device. An example of the residuals using the method state in the above [section 4.6](#) is shown in figure 5.5.1.

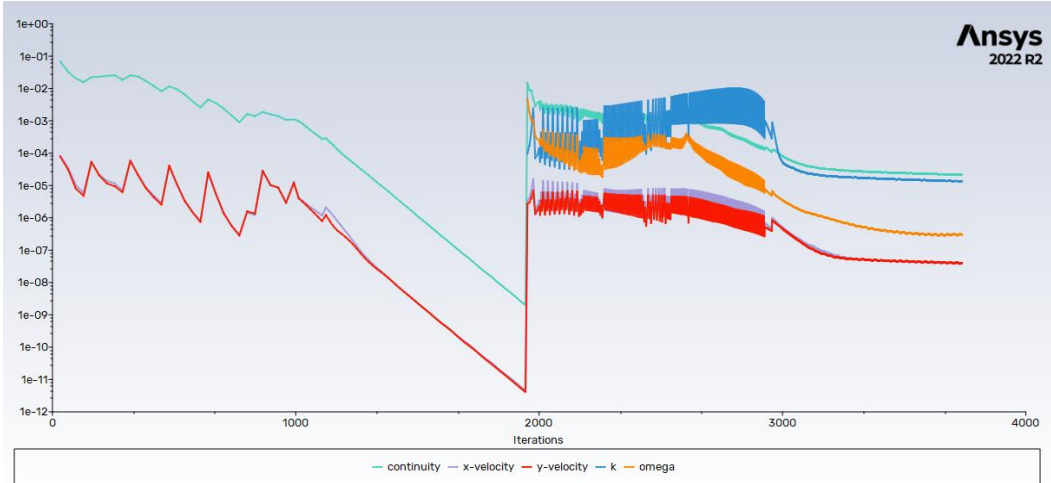


Figure 5.5.1: Scaled Residual of the Simulations at 20° Angle of Attack.

continuity	x-velocity	y-velocity	k	omega
2.1483e-05	3.9448e-08	4.0460e-08	1.3624e-05	2.9657e-07

Table 5.5.1: Final Scaled Residual of the Simulations at 20° Angle of Attack.

By observing the continuity's behaviour on figure 5.5.1, it drops below 1e-6 before steeply increases back up again. This is indicated the swapping of viscous method from S-A scheme to the k- $\omega$  SST. The continuity then settles and stabilized between 1e-4 and 1e-5. Below figure 5.5.2 & 5.5.3 are the lift and drag coefficient against flow time from the same simulation conducted above. A small bump can be observed around flow time of 100000s, corresponding the sudden increment of the residuals. The result are all fluctuating and in a smaller scale of amplitude near the end due to the characteristic of transient method.

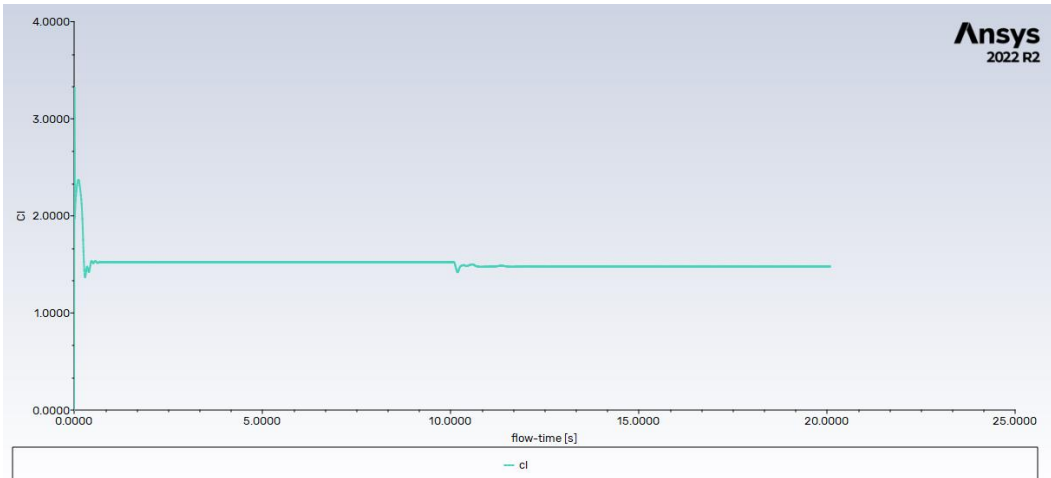


Figure 5.5.2: Lift Coefficient against Flow Time(s)

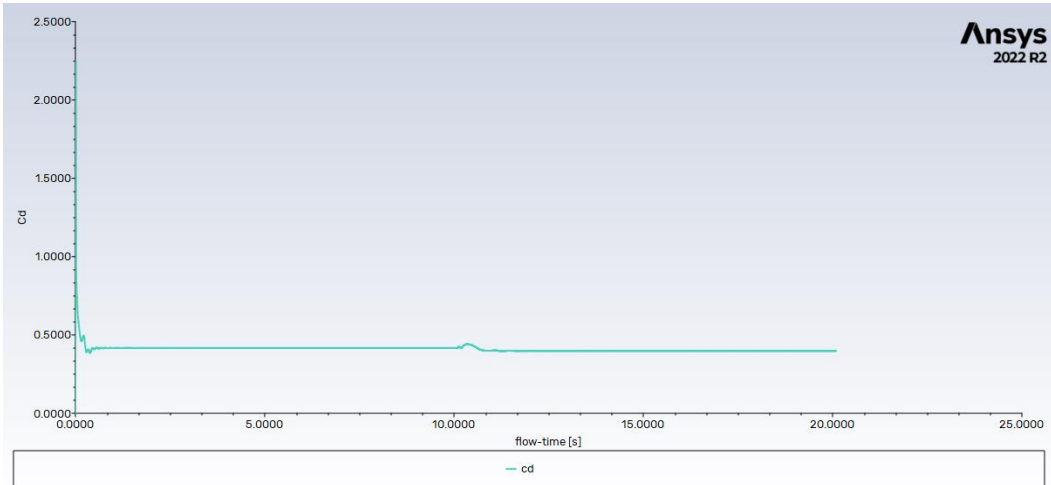


Figure 5.5.3: Drag Coefficient against Flow Time(s).

The result of lift and drag coefficient are plotted and compared with the experimental results from the wind tunnel on figure 5.5.4 & 5.5.5. The graph has shown that the result accomplished using fluent are not exactly accurate when referring to the wind tunnel. The linear approximation of the slope for the results differs by a little. However, by viewing into the individual points, the CFD results is incapable in predicting the stall angle accurately.

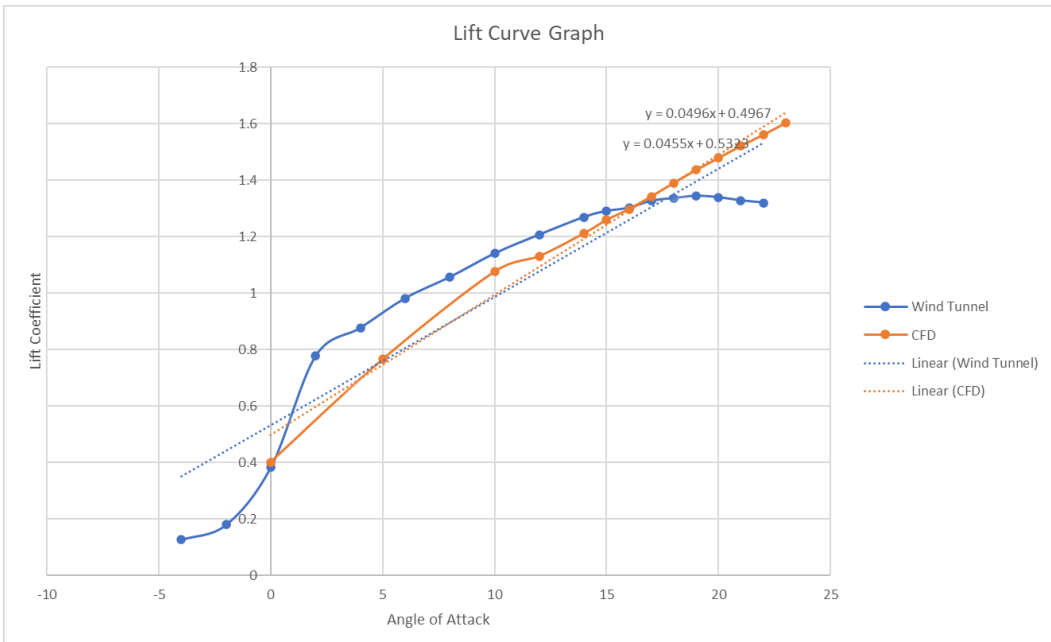


Figure 5.5.4: Comparison of Lift Curve Graph.

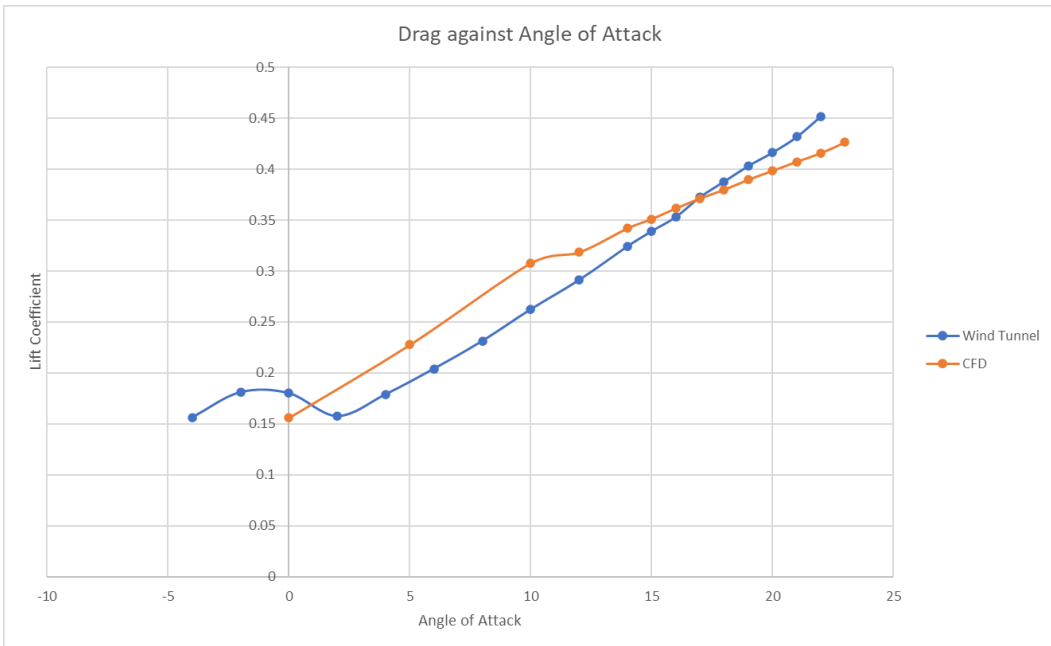


Figure 5.5.5: Comparison of Drag.

The last 4 angle of attack of in figure 5.5.4 & 5.5.5, are already experiencing stalled according to the experimental results. Thus, the value of the lift coefficient produced by Ansys are just to take as references. The convergence criteria of these stalled angle are not as doesn't necessarily goes as small as the other smaller angles. This phenomenon can be concluded through figure 5.5.6 shown below. The continuity curve has reached  $1e-3$  and bounces back up. Comparing the differences between figure 5.5.6 & 5.5.7, it is safe to say that the convergence at lower angle of attack is better. Figure 5.5.8 uses the velocity magnitude contour plot overtime to demonstrate the flow field around the airfoil.

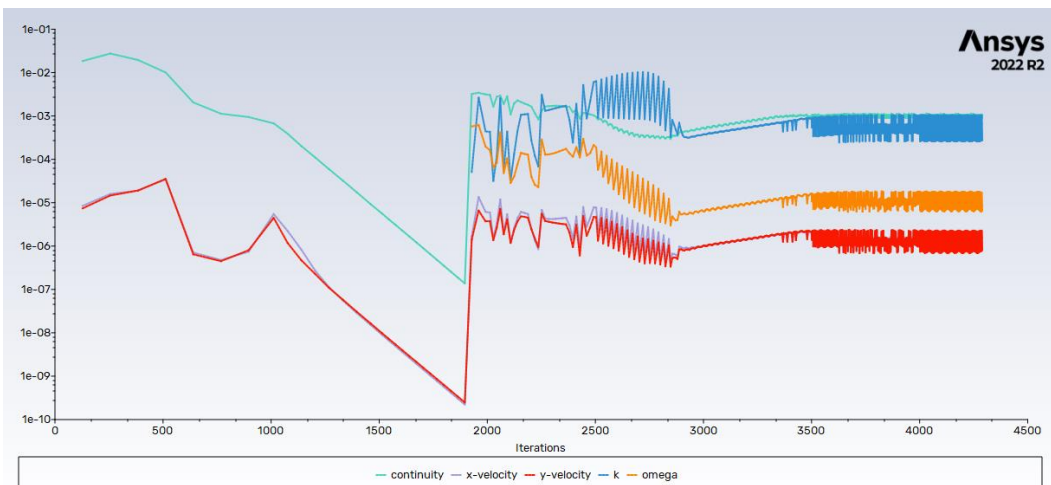


Figure 5.5.6: Residuals of 23 Angle of Attack.

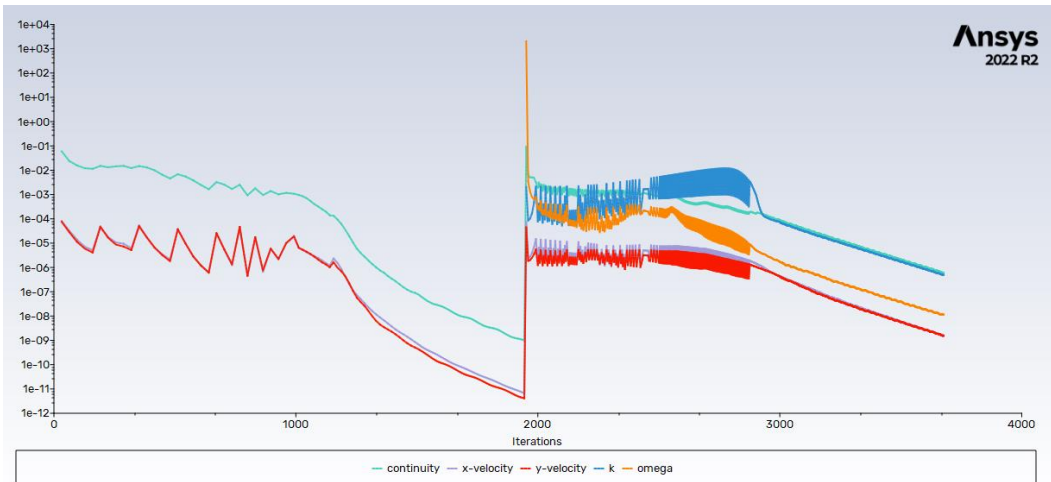


Figure 5.5.7: Residuals of 15 Angle of Attack.

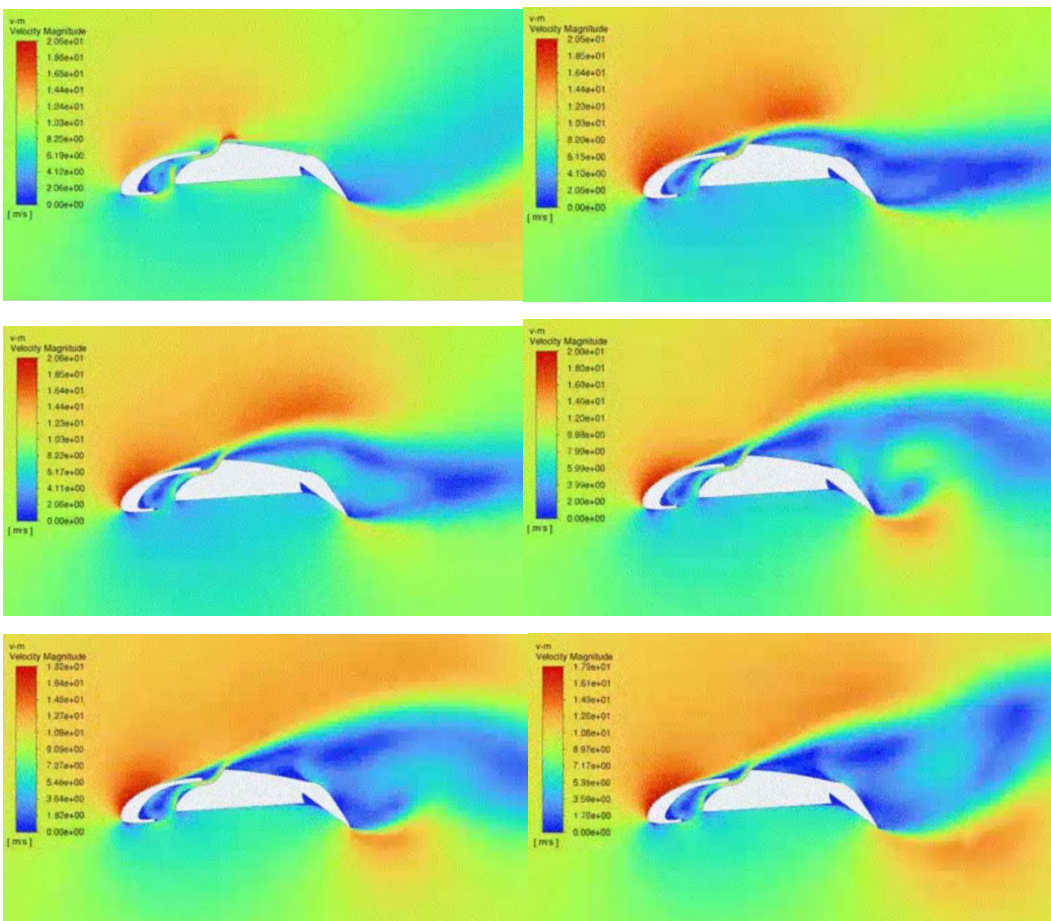


Figure 5.5.8: Example of Velocity Magnitude Contour Plot over Time. (Available at:  
<https://drive.google.com/drive/folders/1P4qg24GLAZOsEQ3WN4YksWxod3BD3EWg?usp=sharing>)

## **6 Discussions & Improvements**

### **6.1 Discussions of the Results**

#### **6.1.1 Wind Tunnel Result**

The result has told that by extending the high lift devices, the lift coefficient only increases by an amount of 9.71% which doesn't reach the expectation. Further looking into the individual contribution of each piece of high lift device, it is found that the deployment of flaps increases the lift coefficient by 14.94%, in this case higher than fully deploying the slats and flaps combined. This is an abnormal discovery as the deployment of flaps can produce higher lift than deploying both the slats and flaps. Thus, by looking into the contribution of the slats itself, we can realise that the deployment of slats decreases the amount of lift that the airfoil is able to gain. This result has clearly not corresponded to the expectation and a further study into the flow field is needed to understand the abnormal performance of the slats.

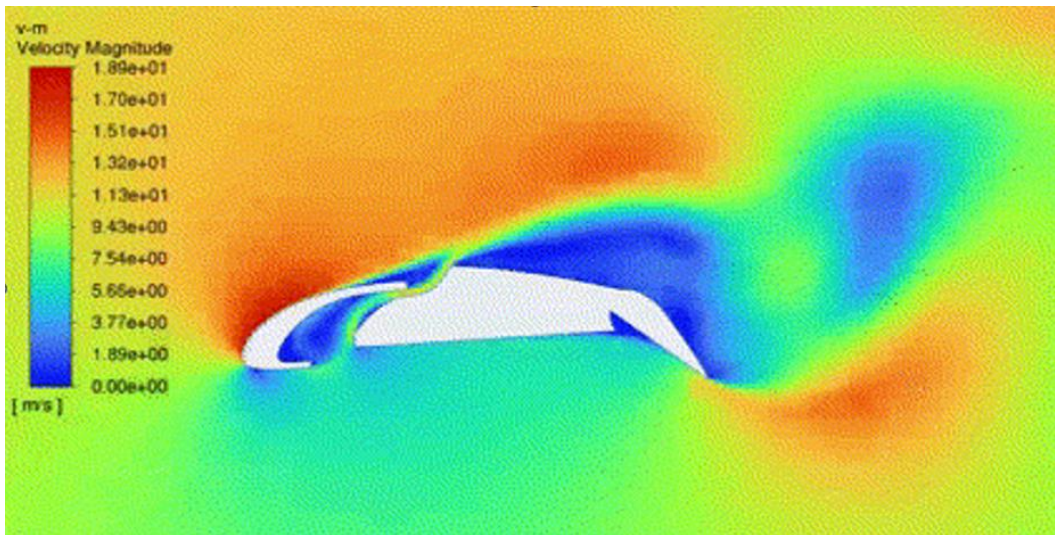


Figure 6.1.1: Velocity Magnitude Contour Plot of the Airfoil at 19° Angle of Attack.

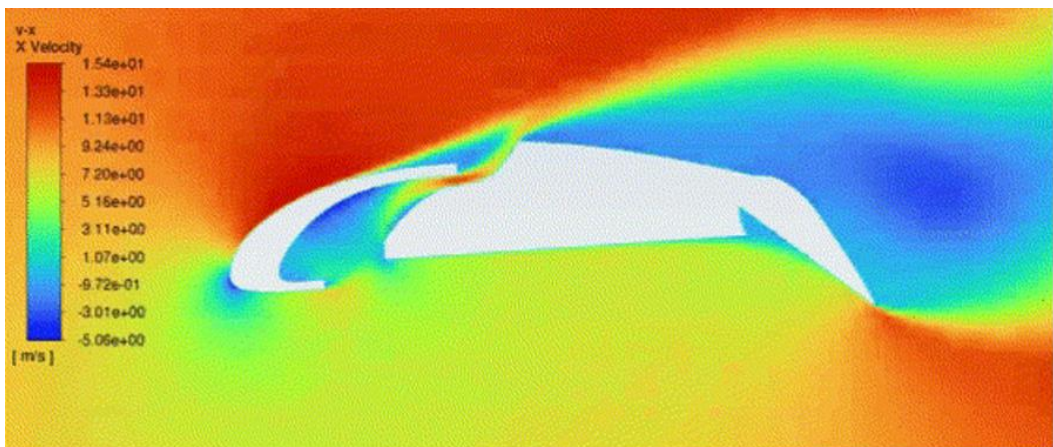


Figure 6.1.2: X-Velocity Contour Plot of the Airfoil at 19° Angle of Attack.

Figures 6.1.1 & 6.1.2 are from animation generated from the same set of simulation conducted in figure 5.5.8. They have shown the velocity magnitude & x-velocity contour plot of the airfoil after fully deflecting all high lift devices respectively. By observing the figures, we can notice that the flow after the leading-edge slats (on the main body region) on the upper surface of the airfoil is the mixture of the low velocity flow from the lower surface and high velocity flow from the upper surface of the leading-edge slats. The mixture of high and low velocity flow is one of the purposes of the slats as it helps to delay the stall of an airfoil. The issue that can be visualised on figures are the mixing of the flow happen with a large angle between the two different velocity flows, which result in a resultant force that causes the mixture of the flows to detach from the airfoil and moves away from the upper surface. This has results in the flow separation happen earlier chordwise and causes the pressure on the upper surface of the main body to increase, causing a sudden loss of lift in the middle part of the airfoil.

Secondly, the reason of the flow separating earlier than expected can still be observed through figures 6.1.1 & 6.1.2. As shown in the figures, the slats' deflecting angle is not big enough to direct the flow straight towards the upper surface of the main body. The flow is directly by the leading-edge slats to impact the main body's cut out edge. As the cut out on the main body consist of a sharp corner on the leading edge, the issue is amplified. This is particularly obvious at high angle of attack.

To solve the problem listed above, a couple changes needed to be made toward the wing. First, the angle of the slats can be increased (making it more cambered) to direct the flow aligning the upper surface of the main body. The sharp edge on the main body cut out can be sand off to create a more rounded edge for the flow to easily attached all the way up to the body.

### 6.1.2 CFD Result

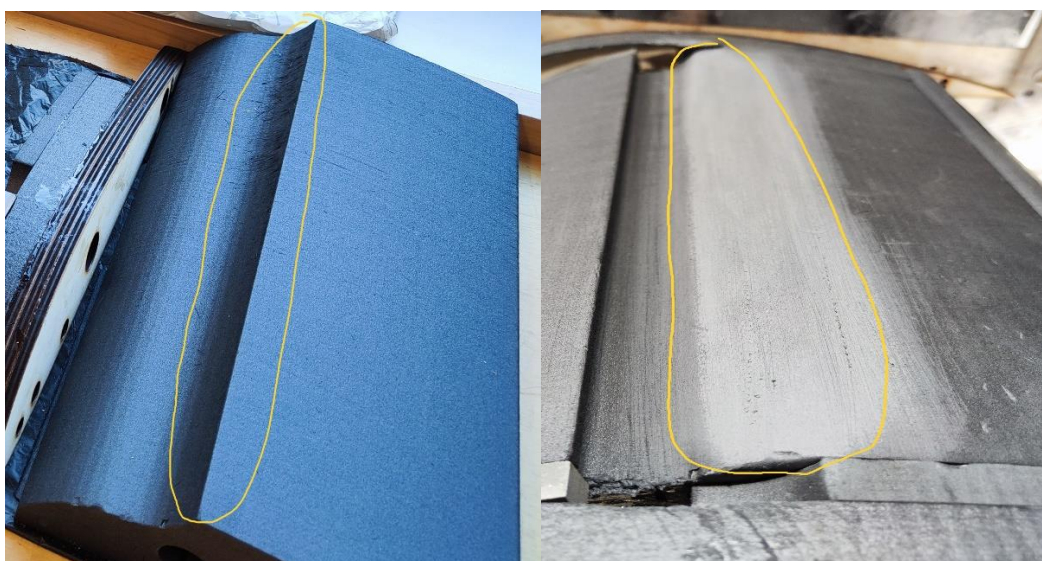
The result has demonstrated the force report of the Ansys differ with the experimental result. Figure 5.5.5 has shown that the lift coefficient predicted by the Ansys at higher angle of attack ( $18^\circ - 23^\circ$ ) continue to rise, while the wind tunnel data show that the wing is experiencing stall. Due to the inconsistent ability of the RANS family solutions to predict the flow field physics of airfoil at near stall angle, the result of the CFD has failed to predict the stall angle precisely. At lower angle of attack, the flow around the airfoil is less turbulent, thus the convergence of the simulations is better while it behaved the opposite on higher angle of attack. This phenomenon is demonstrated by the comparison between figure 5.5.7 and 5.5.8 above. At near stall angle, the boundary

layer of the airfoil consists of a transition range where its behaviour changes from laminar to turbulent. Many RANS code used doesn't help in predicting the transition point, instead it relies on a fully turbulent model or user-defined transition locations [36]. This may lead to the inaccurate prediction of the flow behaviour and false force report.

Beside the issue stated above, it can be realized that the lift coefficient of the CFD presented at 5°- 15° angle of attack is lower than the wind tunnel data referring back to figure 5.5.5. This is due to the simulation are conducted using only a particular part of 2D cross section area of the wing which includes the high lift devices. As introduced on section 6.1.1 above, the high lift devices introduce a sharp corner which is a high pressure point causing the force for the flow to separate. According to "(et al., 1997)" [37], the main causes of the lower value in lift coefficient is predicted to be the simulations are incapable to accurately capture the level of pressure in this region. Inaccurate pressure distribution of the airfoil will directly affect the lift coefficient calculated. This result is also consistent with the finding of (Viken et al., 2003) [38].

## 6.2 Improvement Made

To verify the theory, some modify are made to the wing and an additional test session is conducted.



(a) Main Body Before Modification

(b) Main Body After Modification

Figure 6.2.1: The Wing's Main Body.



Figure 6.2.2: The Wing Tip with Endplate

Figure 6.2.1 shows that the sharp edge of the wing is sanded off to provides the flow a smoother curve to be attached on. The endplate is added to further reduce the wing tip vortices that induced additional drag (Figure 6.2.2). The result of this additional improvement testing is obtained.

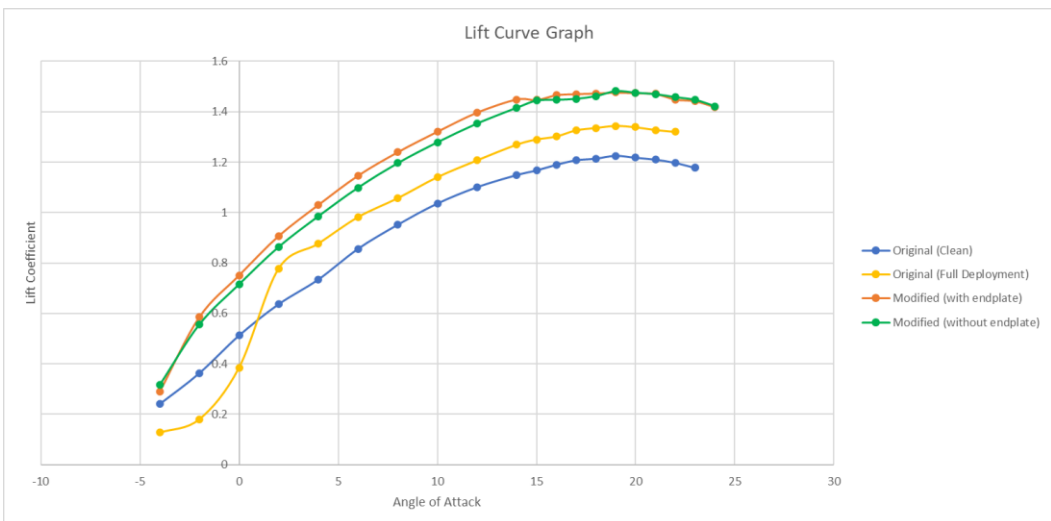


Figure 6.2.3: Comparison of Lift Curve Graph of Different Cases.

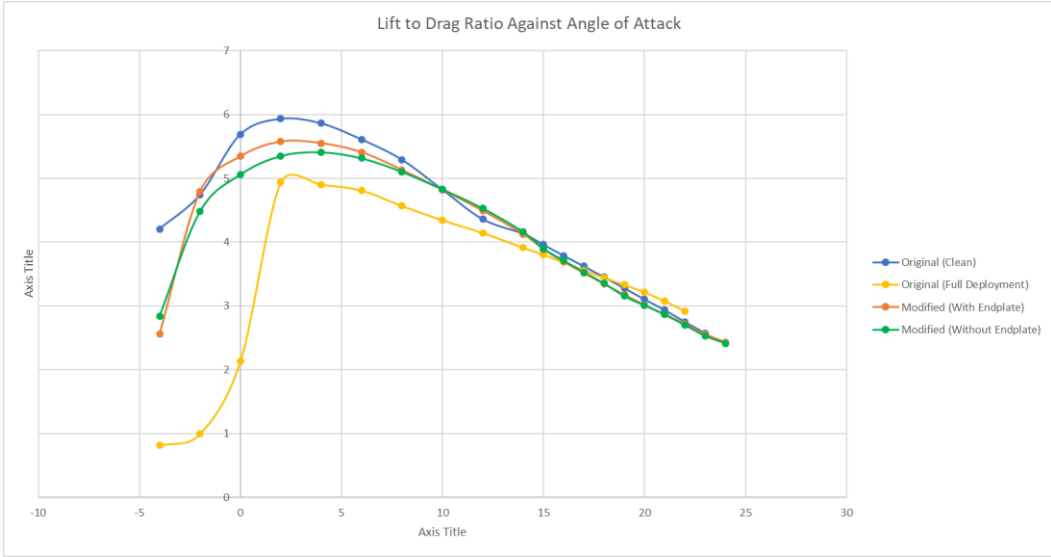


Figure 6.2.4: Comparison of Lift to Drag Ratio Against Angle of Attack of Different Cases.

Figures 6.2.3 & 6.2.4 shows the comparison between the original (unmodified) wing with no deployment (clean), full deployment of high lift devices and the modified wing with and without endplate on full deployment configuration. The modified wing with no deployment is not tested as limit by time. The modified case with endplate (orange line) will be identify as modified case 1, without endplate (green line) as modified case 2.

As figures show, lift coefficient of the modified cases are higher than the original cases. The  $C_{LMax}$  are 1.476 & 1.481, achieved at  $19^\circ$  angle of attack, for the modified case 1 and 2 respectively. They are 20.49% & 20.90% higher than the original clean configuration, 9.82% & 10.19% higher than the original full deployment configuration. The increment in lift coefficient has strengthen the conclusion obtained from the CFD simulations. By smoothening the sharp corner, the flows do attach for a longer period chordwise and thus providing the wing with additional lift.

Looking into figure, the modified case 1 & 2 have increased their maximum L/D ratio when compared to the original fully deployment case. Comparing between modified case 1 and case 2, the case 1 have a slightly higher overall curve. Despite having an additional endplate on the wing tip that supposedly reduce the drag by a significant amount, the difference between modified case 1 and 2 are still small. The drag of a wing can be split into the zero lift drag,  $D_0$  (also known as parasitic drag) and the lift-related drag,  $D_L$  (also known as the induced drag).

$$D = D_0 + D_L \quad (9)$$

A more detailed subdivision can be made is,

$$D = D_{int} + D_{pro} + D_{wav} + D_i + D_m \quad (10)$$

- Interference Drag,  $D_{int}$
- Profile Drag,  $D_{pro}$
- Wave Drag,  $D_{wav}$
- Vortex-Induced Drag,  $D_i$
- Trim Drag,  $D_m$

The term that needs to be considered is only the profile drag,  $D_{pro}$  and the vortex-induced drag,  $D_i$ . The profile drags,  $D_{pro}$  is the sum of skin friction drag and the pressure drag. The vortex induced drag,  $D_i$  are the causes of induced downwash on the main wing and can be reduced by increasing the aspect ratio (Implementing tapered wing increase the aspect ratio).

Thus, the main focus will be around the skin friction drag and the pressure drag. The tests conducted are in conditions of a relatively small wing and low speed, this is a low Reynolds number test recalling the Reynolds number equation (calculated Reynold number of the test is to be around 24364.7).

$$Re = \frac{\rho VL}{\mu} \quad (11)$$

In low Reynolds number the drag is dominant by the skin friction drag. Thus, since the contribution of the pressure drag is small toward the final drag, the impact of the endplate is not significant.



Figure 6.2.5: Visualisation of the Flow on the Main Body

Figure 6.2.5 above shows a visualisation of the flow on the upper surface of the main body right after the slats. The wing in figure is on modified case 1 configuration, meaning that the slats and flaps are fully deployed with the modification state above made. Since the green thread is a very light object, it can follow the flow field and shape accordingly. As shown in the figure, the flow after the slats is more attached on the main body compared to figure 6.1.1.

To further visualize the complete flow around the modified wing, a 2D CFD is conducted. Since the modification of smoothening the corner is made by hand, there's no accurate way construct the modification accurately. Thus, the result regarding the forces of this particular simulation is not considered. The interest in the simulation will be around the improvement of the flow around the cutting out point.

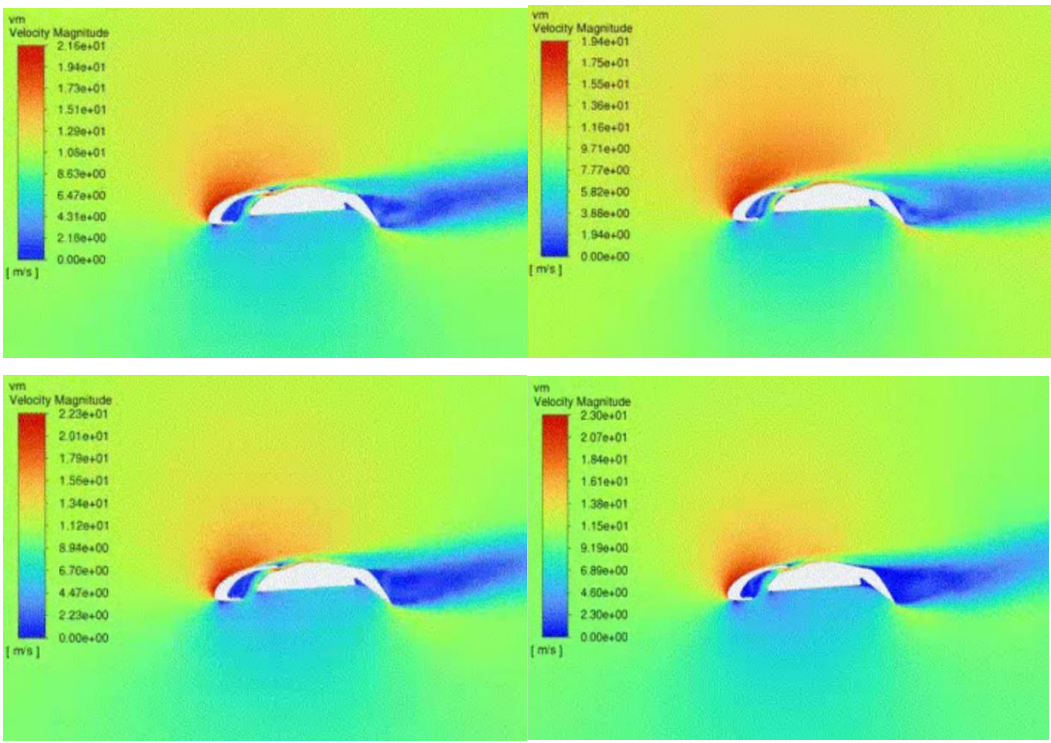


Figure 6.2.6: Velocity Magnitude Contour Plot of the Airfoil After Modifications.

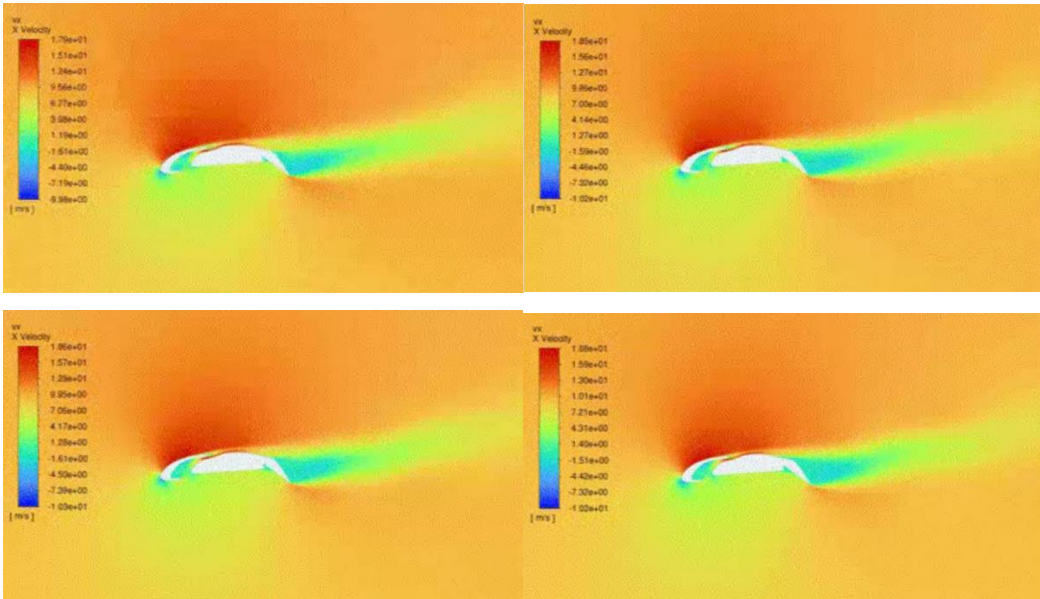


Figure 6.2.7: X-Velocity Contour Plot of the Airfoil After Modifications. (Available at: <https://drive.google.com/drive/folders/1P4qg24GLAZOsEQ3WN4YksWxod3BD3EWg?usp=sharing>)

Figures 6.2.6 & 6.2.7 represents the flow around the airfoil at  $19^\circ$  angle of attack. They are taken from the animation generated from doing transient analysis using Ansys Fluent. By observing them, we can see that the flow after the leading-edge slats is attached to the upper surface. This has enhanced the conclusion reached regarding the increasing of lift.

### 6.3 Additional Test (After Improvement are Made)

During the process of modifying the wing for the second testing, a small modification to the slats mechanism that can change the angle of the slats (e.g., Making it more cambered) that still fits the assembled wing is discovered. To further investigate into the flow field of the wing, a second modification is made toward the wing after the testing above (modified case 1 & case 2).

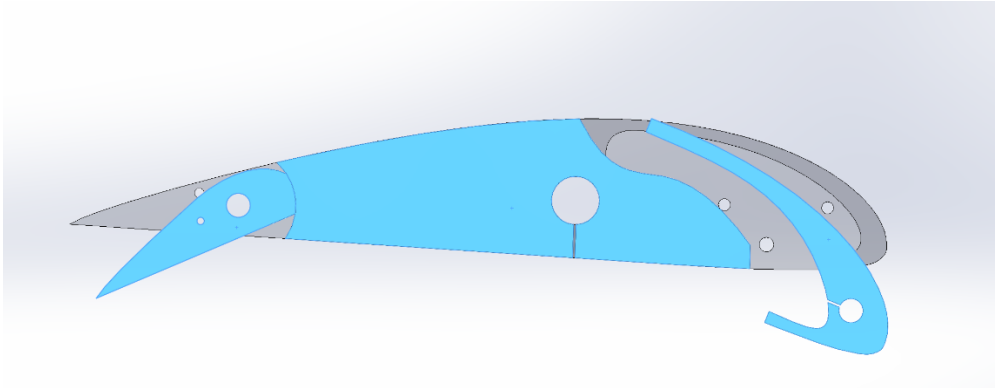


Figure 6.3.1: Cross-Sectional Side View with Change in Slats Implemented.



Figure 6.3.2: The Front View of the Wing with Change in Slats Implemented.

Figures 6.3.1 & 6.3.2 shows the modified wing. The CAD model does not include the modification that is made in section 6.1 (sanding the sharp edge), however the actual wing does include the rounded edge modification as the sanding process can't be undone. The endplate on the wing tip of figure 6.2.2 is also removed for this test. This new modified case will be named as modified case 3.

Although the result of the testing are not satisfying, there's a few information that can be extracted through the analysis of the data.

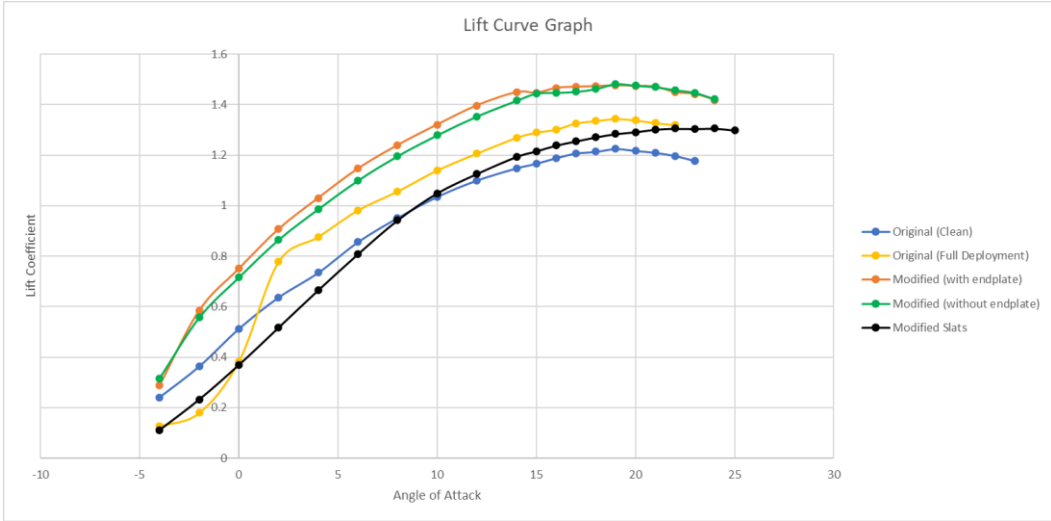
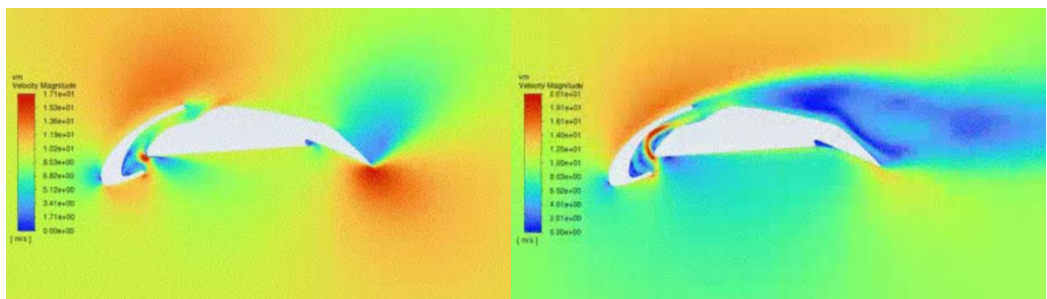


Figure 6.3.3: Lift Curve Graph

The modified case 3 is highlighted in black in figure 6.3.3. Excluding the original clean configuration of the wing, the modified case 3 have a curve lower than all the other case. The  $C_{LMax}$  for this case is 1.306, achieved at 24° angle of attack. The reason that the  $C_{LMax}$  reached at angle of attack higher than any other case is mainly due to the increase of the “by-pass volume” between the slats and the main body of the wing. The increase in the total volume allows more low velocity, high pressure flow to mixed with the upper surface flow which are higher in velocity and lower in pressure. Despite the higher stall angle, the lift coefficient has dropped significantly compared to modified case 1 and 2. The reason resulting this case is the slats angle has increased too much (e.g., too cambered). By observing figure 6.3.1, the upper surface of the leading-edge slats will direct the flow away from the main body with an angle. This ultimately causing the flow to be completely detached from the upper surface, reducing the lift that the wing can originally produce. Below are the CFD approximation regarding the flow around the modified case 3.



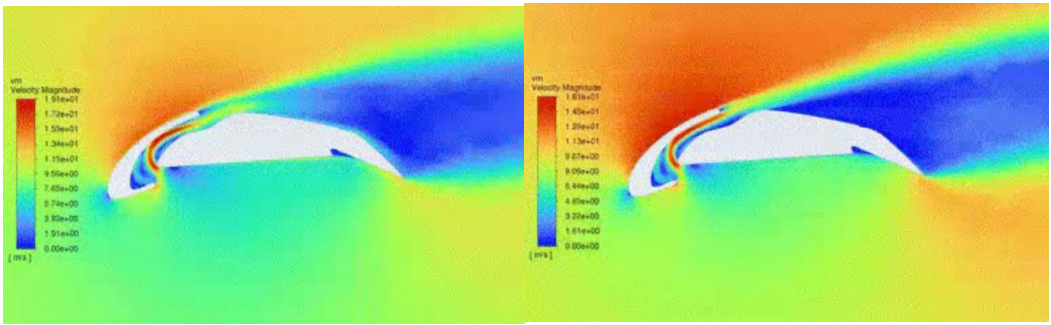


Figure 6.3.4: Velocity Magnitude Contour Plot of the Airfoil of Modified Case 3.([Fig3.4.3](#))

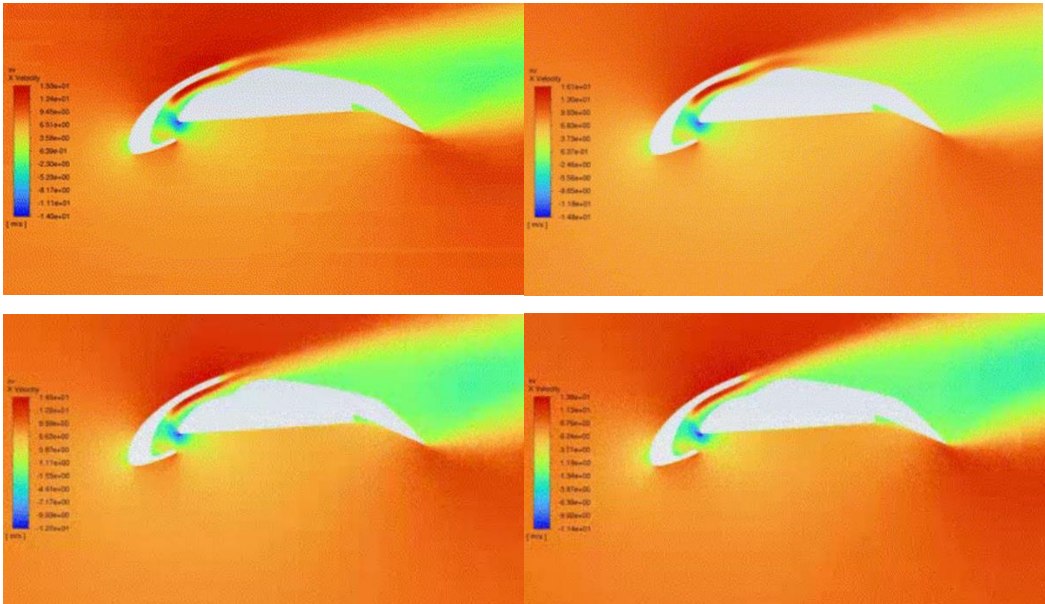


Figure 6.3.5: X-Velocity Contour Plot of the Airfoil of Modified Case 3. (Available at:  
<https://drive.google.com/drive/folders/1P4qg24GLAZOsEQ3WN4YksWxod3BD3EWg?usp=sharing>)

Figures 6.3.4 & 6.3.5 are the velocities contour plot of the modified case 3 at 19° angle of attack, taken from the conducted transient simulation using Ansys Fluent. The figure agrees with the conclusion reached above. Stating the flow after the modified slats has directed to separate the flow from the upper surface.

## 6.4 Extra

A smoke generator is used to visualise the flow at the wing tip. Wing tip vortices, as a form of pressure drag which is caused by the pressure difference between the upper and lower surface is demonstrated in figure below. The endplate applied above can reduce the effect of the vortices.



Figure 6.4.1: Wing Tip Vortices. (Available at:

<https://drive.google.com/drive/folders/1P4qg24GLAZOsEQ3WN4YksWxod3BD3EWg?usp=sharing>)

Unfortunately due to the smoke machine's technical issue, the smoke are not able to reach the level of the high lift devices else it would have been easier to visualize the flow demonstrated using CFD animations.

## **7. Conclusions**

The wing made using modified Clark-Y airfoil have its maximum lift coefficient of 1.225 at  $19^\circ$  angle of attack. The result has successfully shown that despite the problems that the slat introduces, the high-lift devices does increase the overall lift generated by the wing with maximum increase of 20.9%. Accounting for the unexpected issue with the slat, the overall lift to drag ratio after deploying the devices are similar to the clean configurations. Thus, with a carefully design slat, it is safe to say that the L/D ratio will be increase from the clean wing.

The project has introduced several major constraints towards the designing process of the high-lift systems. The angle of deflection of the leading-edge devices, is one of the major concerns. The results have demonstrated that the flow over is extremely sensitive toward the geometry after the slat. More process should be done beforehand to align the flow of each element of the airfoil to ensure the boundary layer stay attached longer. The result of the individual testing of the flaps suggested that the flaps can increase the lift by a significant amount. To further improve the performance, an amount of the slotted flaps can be increased as well as the angle of deflection of the flaps.

In addition to increase the accuracy of the CFD, it is recommending the use of a finer mesh with smaller wall  $y$  plus in exchange in more computational cost. A Large-Eddy Simulation (LES) approach can be made after the RANS simulation to improve the prediction of the large turbulent motions thus providing a better force prediction. A better design of the high lift devices will also help the result to converge better as the flow will be steadier with less and later separations.

## **8. References**

1. *2.972 how an airfoil works.* Available at:  
<https://web.mit.edu/2.972/www/reports/airfoil/airfoil.html>(Accessed: April 7, 2023).
2. *Camber* (no date) *SKYbrary Aviation Safety.* Available at:  
<https://www.skybrary.aero/articles/camber> (Accessed: April 7, 2023).
3. Babinsky, H. (2003) "How do wings work?," *Physics Education*, 38(6), pp. 497–503. Available at: <https://doi.org/10.1088/0031-9120/38/6/001>.
4. *how do wings work? - department of engineering.* Available at:  
<https://www3.eng.cam.ac.uk/outreach/Project-resources/Wind-turbine/howwingswork.pdf> (Accessed: April 7, 2023).
5. Admin, J.Y.P. (2021) *How does an airplane generate lift force?* , JYP. JYP. Available at: <https://www.journalofyoungphysicists.org/post/how-does-an-airplane-generate-lift-force-review> (Accessed: April 7, 2023).
6. *Coanda effect* (no date) *Coanda Effect - an overview / ScienceDirect Topics.* Available at: [https://www.sciencedirect.com/topics/earth-and-planetary-sciences/coanda-effect#:~:text=\(The%20Coanda%20effect%20is%20the,for%20which%20it%20was%20intended](https://www.sciencedirect.com/topics/earth-and-planetary-sciences/coanda-effect#:~:text=(The%20Coanda%20effect%20is%20the,for%20which%20it%20was%20intended). (Accessed: April 7, 2023).
7. Obiga, O. (2018) *Investigation of the performance of a slotted aerofoil at low Reynolds Numbers, Investigation of the performance of a slotted aerofoil at low Reynolds numbers - Nottingham ePrints.* Available at:  
<http://eprints.nottingham.ac.uk/46841/> (Accessed: April 7, 2023).
8. *B777 High Lift Control System* (no date) *Flight To Success.* Available at:  
<https://karlenepetitt.blogspot.com/2017/10/b777-high-lift-control-system.html> (Accessed: April 7, 2023). (S&f Pic)
9. *Use of flaps - faasafety.gov* (no date). Available at:  
<https://www.faasafety.gov/files/gslac/courses/content/35/376/Use%20of%20Flaps.pdf> (Accessed: April 7, 2023).
10. J.B. Russell MSc (2007) *Performance and Stability of Aircraft, ScienceDirect.* Butterworth-Heinemann. Available at:  
<https://reader.elsevier.com/reader/sd/pii/B9780340631706500037?token=60>

- 774B78FCF2616C21C22B743C0EF50C676E98294455B98138CBC709C0CB61A  
 C11ED2A3BE667B1D7A31214E2E9A4CE7A89&originRegion=eu-west-  
 1&originCreation=20230401141734 (Accessed: April 7, 2023).
11. M. Klein(2007) *Sensitivity of aerodynamic optimization to parameterized target functions*, *ScienceDirect*. Elsevier Science Ltd. Available at:  
<https://reader.elsevier.com/reader/sd/pii/B9780080439518500436?token=82EAFF8846E406212009C72E0ECDC5994BB77DDDA66A38B3163C920A075DE6E68C5BA795D5B07E82CFDF2E6A8536C127&originRegion=eu-west-1&originCreation=20230401141610> (Accessed: April 7, 2023).
12. Het Bhavsar a et al. (2022) *Multi-element airfoil configuration for hawt: A novel slot design for improved aerodynamic performance*, *Materials Today: Proceedings*. Elsevier. Available at:  
<https://reader.elsevier.com/reader/sd/pii/S2214785322052634?token=6B97A16FCAA4A62552B1B16C3DA2F50229A90BC5E95A792AB0B36D11245F04B57BAEF136E585D2F7FB793ACD96EB9BD2&originRegion=eu-west-1&originCreation=20230401114512> (Accessed: April 7, 2023).
13. (no date) *Leading Edge Flap - an overview* / *ScienceDirect Topics*. Available at: <https://www.sciencedirect.com/topics/engineering/leading-edge-flap> (Accessed: April 7, 2023). (slats Pic)
14. Mahoney, A.B. (2017) *Slats, The Physics Water Cooler*. Available at:  
<https://physicswatercooler.wordpress.com/tag/slats/> (Accessed: April 7, 2023).
15. David Fisher, Robert C. Nelson and Flint O. Thomas (1996) *Key Topics for High-Lift Research: A Joint Wind Tunnel / Flight Test Approach*, NASA. NASA-Ames University Consortium Joint Research Interchange. Available at:  
<https://ntrs.nasa.gov/api/citations/19970003008/downloads/19970003008.pdf> (Accessed: April 7, 2023).
16. MACK, M. and MCMASTERS, J. (1992) "High Reynolds number testing in support of Transport Airplane Development," *17th Aerospace Ground Testing Conference* [Preprint]. Available at: <https://doi.org/10.2514/6.1992-3982>. FIGURE3,8
17. John C. Lin et al. (no date) *High Lift Common Research Model for Wind Tunnel Testing: An Active Flow Control Perspective*, NASA . NASA Langley

Research Center, Hampton, VA, 23681, USA. Available at:  
<https://ntrs.nasa.gov/api/citations/20170001029/downloads/20170001029.pdf> (Accessed: April 7, 2023).

18. *Flaps* (no date) *SKYbrary Aviation Safety*. Available at:  
<https://www.skybrary.aero/articles/flaps> (Accessed: April 7, 2023). FIGURE 3.7

19. *Krueger flaps* (no date) *SKYbrary Aviation Safety*. Available at:  
<https://www.skybrary.aero/articles/krueger-flaps> (Accessed: April 7, 2023). FIGURE 3.7

20. *K-Omega and K-omega SST: Global settings* (2021) *SimScale*. Available at:  
<https://www.simscale.com/docs/simulation-setup/global-settings/k-omega-sst/> (Accessed: April 7, 2023).

21. *Pressure-velocity coupling* (no date) *Ansys Fluent 12.0 theory guide* . Available at:  
<https://www.afs.enea.it/project/neptunius/docs/fluent/html/th/node373.htm> (Accessed: April 7, 2023).

22. *Pressure drag* (no date) / *ScienceDirect Topics*. Available at:  
<https://www.sciencedirect.com/topics/earth-and-planetary-sciences/pressure-drag> (Accessed: April 7, 2023).

23. F.R. Menter, A. Matyushenko and R. Sechner (no date) *Best Practice: RANS Turbulence Modeling in Ansys CFD, Ansys | Engineering Simulation Software*. Available at:  
<https://www.ansys.com/content/dam/amp/2022/february/asset-creation/best-practices-campaign/Best%20Practice-Rans%20turbulence%20modeling%20in%20Ansys%20CFD.pdf>.

24. *Choosing the pressure-velocity coupling method* (no date) *Ansys Fluent 12.0 user's guide*. Available at:  
<https://www.afs.enea.it/project/neptunius/docs/fluent/html/ug/node785.htm#sec-uns-simple-vs-simplec>.

25. *Aerodynamic Lift and Drag and the Theory of Flight* (no date) *Electropaedia* . Available at: [https://www.mpoweruk.com/flight\\_theory.htm](https://www.mpoweruk.com/flight_theory.htm).

26. *Form drag* (no date) *SKYbrary Aviation Safety*. Available at:  
<https://www.skybrary.aero/articles/form-drag> (Accessed: April 7, 2023).

27. *Friction drag* (no date) SKYbrary Aviation Safety. Available at:  
<https://www.skybrary.aero/articles/friction-drag#:~:text=Friction%20Drag%2C%20also%20known%20as,the%20square%20of%20the%20velocity.> (Accessed: April 7, 2023).
28. Jha, S. et al. (2018) “Effect of Reynolds number on the aerodynamic performance of NACA0012 aerofoil,” *IOP Conference Series: Materials Science and Engineering*, 377, p. 012129. Available at:  
<https://doi.org/10.1088/1757-899x/377/1/012129>.
29. Jain, S., Sitaram, N. and Krishnaswamy, S. (2015) “Effect of Reynolds number on aerodynamics of airfoil with gurney flap,” *International Journal of Rotating Machinery*, 2015, pp. 1–10. Available at:  
<https://doi.org/10.1155/2015/628632>.
30. R. Radespiel, L. Bertsch and W. Heinze (no date) *HIGH-LIFT RESEARCH FOR FUTURE TRANSPORT AIRCRAFT*, core.ac.uk. Technische Universität Braunschweig. Available at: <https://core.ac.uk/download/pdf/86640071.pdf> (Accessed: April 7, 2023).
31. ARRA, A., ANEKAR, N. & NIMBALKAR, S. 2021. Aerodynamic effects of leading edge (LE) slats and slotted trailing edge (TE) flaps on NACA-2412 airfoil in prospect of optimization. *Materials Today-Proceedings*, 44, 587-595.
32. TIMMER, W. A. & BAK, C. 2013. Aerodynamic characteristics of wind turbine blade airfoils. *Advances in Wind Turbine Blade Design and Materials*, 109-149.
33. VAN DAM, C. P. 2002. The aerodynamic design of multi-element high-lift systems for transport airplanes. *Progress in Aerospace Sciences*, 38, 101-144.
34. VAN DAM, C. P. 2002. The aerodynamic design of multi-element high-lift systems for transport airplanes. *Progress in Aerospace Sciences*, 38, 101-144.
35. Ashish Ghimire (no date) “POWER SIZING APPROACHES AND METHODS FOR TRAILING EDGE HIGH LIFT CONTROL DEVICES DURING PRELIMINARY PHASE OF AIRCRAFT DEVELOPMENT .”
36. Shelton, A. et al. (2005) “Improving the CFD predictions of airfoils in stall,” *43rd AIAA Aerospace Sciences Meeting and Exhibit* [Preprint]. Available at: <https://doi.org/10.2514/6.2005-1227>.
37. Gianluca Iaccarino et al. (1997) *RANS simulation of the separated flow over a bump with active control*. Stanford University. Available at:  
<https://web.stanford.edu/group/ctr/ResBriefs03/iaccarino2.pdf>.
38. Viken, S. et al. (2003) “Flow control analysis on the hump model with RANS Tools,” *41st Aerospace Sciences Meeting and Exhibit* [Preprint]. Available at: <https://doi.org/10.2514/6.2003-218>.

